Hindawi
Geofluids
Volume 2019, Article ID 9582359, 23 pages
https://doi.org/10.1155/2019/9582359

Research Article

Petrophysical Properties and Microstructural Analysis of Faulted Heterolithic Packages: A Case Study from Miocene Turbidite Successions, Italy

Hannah Riegel[1,2], **Miller Zambrano**[1,2,3], **Fabrizio Balsamo**[4], **Luca Mattioni**[5] and **Emanuele Tondi**[1,2,3]

[1]*School of Science and Technology-Geology Division, University of Camerino, Via Gentile III da Varano, 7, Camerino 62032, Italy*
[2]*Reservoir Characterization Project, Italy*
[3]*GeoMORE s.r.l, Via Gentile III da Varano, 7, Camerino 62032, Italy*
[4]*Department of Chemistry, Life Sciences, and Environmental Sustainability, Parma University, Campus Universitario, Parco Area delle Scienze 157/A, I-43124 Parma, Italy*
[5]*Neptune Energy International S.A. Faubourg de l'Arche, 1 Place Samuel de Champlain, La Défense, Paris 92930, France*

Correspondence should be addressed to Hannah Riegel; riegelhb@gmail.com

Received 30 November 2018; Revised 17 March 2019; Accepted 9 April 2019; Published 2 June 2019

Academic Editor: Ye Zhang

Geofluid reservoirs located in heterolithic successions (e.g., turbidites) can be affected by vertical and lateral compartmentalization due to interbedded fine-grained facies (i.e., shale, siltstones) and the presence of faults, respectively. A fault can behave as a conduit or barrier to fluid flow depending on its architecture and the individual hydraulic behavior of its components (i.e., fault core, damage zone). The fault core, normally composed by fault rock or smeared clay material, commonly acts as a flow inhibitor across the fault. Fault-related fractures (macro- and microscopic) in the damage zone generally increase the permeability parallel to the fault, except when they are cemented or filled with gouge material. Although macrofractures (which define the fracture porosity) dominate fluid flow, the matrix porosity (including microfractures) begins to have a more important role in fluid flow as the aperture of macrofractures is occluded, particularly at greater depth. This study investigates the variation in matrix permeability in fault zones hosted in heterolithic successions due to fault architecture and stratigraphy of host rock (i.e., sand-rich turbidites). Two key areas of well-exposed, faulted Miocene turbidites located in central and southern Italy were selected. For this study, six separate fault zones of varying offset were chosen. Each impacts heterolithic successions that formed under similar tectonic conditions and burial depths. Across the selected fault zones, an extensive petrophysical analysis was done in the field and laboratory, through air permeameter measurements, thin section, and synchrotron analysis in both host rock, damage zone, and fault core. Results suggest that the amount and distribution of clay layers in a heterolithic sequence affects fluid flow across the fault, regardless of fault offset.

1. Introduction

Heterolithic successions (e.g., sand-rich turbidites) represent important deep-water targets for oil and gas exploration due to their considerable lateral continuity and high sand volume [1, 2]. Despite a high net-to-gross value, the production of hydrocarbon in these reservoirs can be affected by vertical and lateral compartmentalization due to interbedded fine-grained facies (i.e., shale, siltstones) and faults, respectively [3, 4].

The control exerted by the fault on fluid flow is defined by three main elements: (1) juxtaposition, (2) fault rock, and (3) the surrounding damage zone [5–13]. The fault rock may often diminish the fluid flow perpendicular to the fault, depending on its mineral composition, grain size, and cementation (e.g., [7, 13]). In a heterolithic succession, the

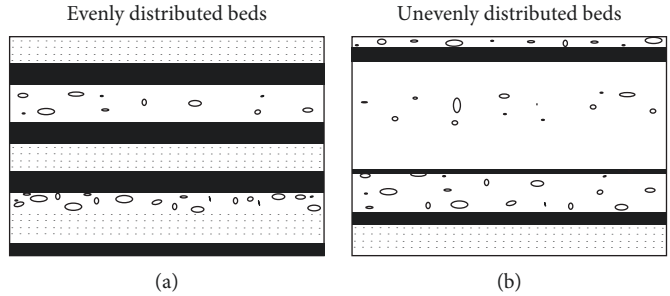

Figure 1: The two-types of packages found at the key sites: (a) evenly distributed beds contain a relatively even distribution of interbedded clay layers (in black) throughout the package; (b) unevenly distributed beds contain a sparse or random arrangement of clay beds relative to the other lithofacies (e.g., siltstone, sandstone, conglomerates) present.

presence of clay within the fault core may also contribute to the sealing behavior of the fault (clay smearing process) [14–17]. In these reservoirs, the stratigraphy may exert a primary control on the fracture intensity distribution in both host rock (diffuse deformation) and fault zones (localized deformation) [18–23]. In general, fractures within the damage zone are more abundant in comparison to the host rock as the distance to the fault core decreases [24–28]. The fractures in the damage zone may enhance the fluid flow parallel to the fault if they are opened (e.g., joints, partially cemented joints) and connected. However, they may inhibit the cross-flow when closed by secondary mineralization, fault gouge, or deformation banding [13, 29–33]. The permeability associated to fractures within the damage zone may change over time due to the interplay of coseismic fracturing, pressure variation, and sealing/healing [34–37].

Despite the fact that macrofractures (which define the fracture porosity) generally dominate fluid flow within the fault zone, the matrix porosity (including microfractures) may start to have a more important role to fluid flow as the aperture of macrofractures decreases, particularly at greater depths [37, 38]. Matrix porosity (and permeability) can be increased at low stress levels due to the development of microfractures, even though the regional stresses are below the fracture strength of the rock [39–41]. Like fracture porosity, matrix porosity can increase toward the main fault surface due to a higher density of fault-related microfractures [37, 42]. The control exerted by the stratigraphy (lithology and their relative thickness distribution) on matrix permeability distribution in fault zones hosted in heterolithic succession has been poorly investigated.

This study investigates the matrix permeability variation in fault zones hosted in heterolithic successions due to fault architecture and stratigraphy of host rock (i.e., even vs. unevenly distributed beds; Figure 1). The proposed methodology consists on combining in situ air permeameter measurements with thin section and X-ray computed microtomography (X-ray microCT) image analysis in host rock, damage zone, and fault core. The evaluation of fault zone architecture, fault slip, and lithofacies associations is completed at each outcrop. The study is focused in two key outcrop areas located in central and southern Italy, where the Macigno Formation and the Cilento Group are exposed (Figure 2). Despite the geographic distance, both sand-rich turbidites formed under similar tectonic conditions and shared similar structural evolution.

2. Geological Setting

This study was developed in two different locations: (i) Livorno-Piombino (Figure 2(a)) and (ii) San Marco di Castellabate (Figure 2(b)). Despite the distance (~530 km), the heterolithic successions exposed in both areas were formed under similar tectonic conditions resulting in similar structural evolution [43–46].

2.1. Livorno–Piombino Area. The first study area is located within the Macigno Formation, which is made up of Late Oligocene to Miocene turbidite deposits [49]. Part of a diachronically migrating foredeep system, the Macigno Formation was laid down in a compressional setting, most likely a thrust-top basin [43, 44]. According to paleogeographic reconstructions, the Macigno Basin was 150-200 km wide and occupied a part of the present Ligurian and Tyrrhenian seas [43]. It was then deformed and organized into several thrust units in multiple tectonic events during the Miocene and the Pliocene [50, 51]. While the orogenic front and foredeep basin were migrating, the proximal turbidite facies of the transversal feeders (named as the "Macigno costiero") were substituted by distal turbidite facies of the longitudinal basin feeders (named as the "Macigno appenninico") [43, 44, 49]. Faults in the area are characterized as NW-SE-striking dip slip faults with minor WSW-ENE strike slip faults characterized by different degrees of maturity [52–54].

The Macigno costiero primarily crops out between the towns of Livorno and Piombino in central Italy (Figure 2(a)). It is a quartz- and feldspar-rich siliciclastic succession made up of Late Oligocene-Early Miocene foredeep-related sediments of thickness ranging from 0.5 to 3.0 km. It is dominated by turbiditic sandstones with minor shales and siltstones, rare conglomerates, and some detrital limestones [49]. These turbidites flowed transversely, with respect to the basin, and were deposited in a wide foredeep basin located close to the orogenic wedge where sedimentation first developed in the internal zones [53].

In coastal outcrops, the Macigno costiero contains fossils and carbonates due overall to proximal turbidite facies

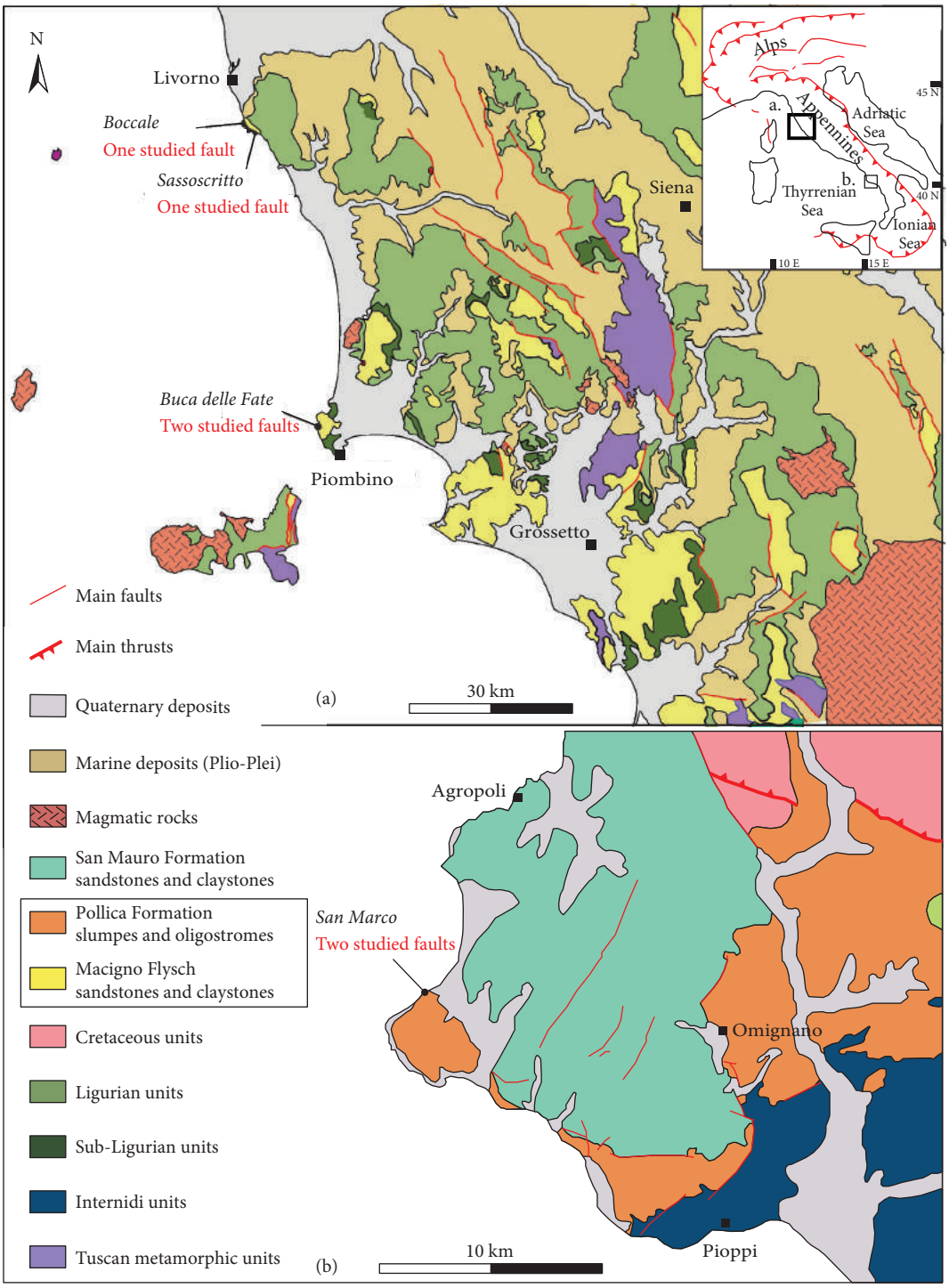

Figure 2: Locations of study areas along with key sites denoted in italics. The focused geologic formations are denoted inside the rectangle. (a) Livorno-Piombino area [47], (b) Agropoli-Pioppi area (San Marco di Castellabate) [48].

instead of distal [55, 56]. The Macigno costiero sandstone beds, from cm- to m-thick and gray-colored (ochre-weathering), are mainly made up of quartz and feldspar grains (plagioclase and k-feldspar), as well as white mica and chlorite grains, and crystalline lithics consisting of igneous and metamorphic rock fragments [55–57]. The cements of sandstones are mainly argillaceous-phyllosilicates, calcite, and to a lesser degree quartz [57]. At the Bay of Baratti (Buca delle Fate site; Figure 2(a)), carbonate lithics are present. Gneiss and quartz- and muscovite-rich schists are the most common metamorphic lithic grains [58]. The sandstones are classifiable as feldspathic litharenite [57]. In Calafuria (sites Boccale, Sassoscritto, and Scogli di Calafuria; Figure 2(a)), volcanic grains have an

intermediate composition [58]. Like Baratti, gneiss and quartz-muscovite schists are the prevalent metamorphic grains [58].

2.2. San Marco di Castellabate. The second study area is located in southern Italy between the towns of Agropoli and Pioppi, where the Cilento Group is exposed (Figure 2(b)). The Cilento Group was deposited in the Early Miocene (Late Burdigalian to Serravallian) and unconformably overlays the tectonized Ligurian accretionary complex [59–62]. These tectonized units represent the beginning of the Apennine mountain-building [45, 46].

Structurally, the area is characterized by left lateral wrench faults trending WNW-ESE [52]. The tectonized Ligurian units that are overlain by the Cilento Group are cut by a series of SE down-throwing listric faults [52, 63]. Shortening is also present, most noticeably in the sediments affected by the overthrusting of the Lagonegro Units onto the Cilento Group [52, 64].

The predominantly sandstone Cilento Group formed as a wedge-top basin succession [45, 46, 62, 64] and is sourced mainly from a siliciclastic Calabrian basement [65]. The Cilento Group contains a mix of heterogeneous strata including beds with fine-grained matrix with detached layers and pebble-boulder clasts, alternating clay layers, and sandstones, making up the oldest thrust-top syntectonic strata represented in the southern Apennines [60].

For this study, outcrops from the Pollica Formation, the oldest formation pertaining to the Cilento Group (Langhian), are studied. [66]. Deposited on an episutural basin of pre-Burdigalian strata [67, 68], both formations are primarily composed of siliciclastic arenites and marly siliciclastic arenitic turbidites [63]. The Pollica Formation ranges in thickness from 350 to 600 m and is made up of two members, (1) the Cannicchio Member and (2) the Pollica Sandstones [66]. The Cannicchio Member is primarily made up of mainly siliciclastic arenites with lesser clay facies dispersed throughout (sandstone/pelite ratio < 1) [66]. It is characterized by synsedimentary deformation and debris flows with a muddy matrix. The Pollica Sandstones Member is the thicker of the two, varying in thickness between 200 and 400 m. It is characterized by coarser-grained material (sandstone/pelite ratio > 1) in relation to the Cannichio Member, with several cycles of coarsening up. Debris flows are also present [66].

3. Methods

3.1. Air Permeameter Measurements. Field-based direct permeability measurements (646 in total) were carried out in fault zones located in both study areas (Table 1). In the Livorno-Piombino area, 3 sites were analyzed: (i) Boccale and (ii) Sassoscritto, which represent channel fill facies, and (iii) Buca delle Fate which represents channel-levee facies. In San Marco di Castellabate, a succession composed of channel-levee environment and less turbulent environments associated with marl beds is exposed.

Permeability measurements were taken in vertical sections (cliffs) along transects of 2-3 m-long across six faults (including host rock, damage zone, and fault core) crosscutting different lithofacies (i.e., sandstones, siltstones, and shale). Where possible, measurements were taken perpendicular to the fault plane as well. Measurements were performed using a TinyPerm II Portable Air Permeameter (manufactured by New England Research) which provides reliable values from 10^{-4} to 10 Darcy [30, 69–71]. To avoid bias due to surface irregularities and weathering, sampling sites were cleaned and cleared of detritus that would influence the measurements [30]. Macrofractures may influence permeability measurements and so were avoided. A silicon ring (5 mm of diameter) was used to avoid air leaking from the minipermeameter nozzle, which is far smaller than the width of fault cores sampled. In order to convert the TinyPerm II output value (T) to standard units of permeability (i.e., Darcy, D), we used the equation provided in the manual of the device [71]:

$$k = \frac{10^{(T-12.8737/-0.8206)}}{1000}, \quad (1)$$

where T is the output value (unitless) of the device, and k corresponds to the permeability in Darcy, (D).

3.2. Structural Analysis. Studied faults are divided into three different groups based on architecture, not offset (Figure 3; Table 1). Incipient faults are characterized by a single fault plane with minimal fault core (<3 cm, not including shale gouge). Well-developed faults are characterized by throughgoing slip surfaces associated with well-developed splays and fault core. Faults deemed "complex" are also found at the study sites. They characteristically have a well-developed fault core (often with cataclasite/clay smear) and an extensive, thick damage zone. Three or more fault planes are often present.

3.3. Lab-Based Analysis

3.3.1. Thin Section Observations, Density, and Porosity Analysis. Samples for thin section and laboratory analysis were collected at each location in order to study properties like microstructural features, mineralogy, and grain orientation that would impact permeability. Samples were taken from the host rock of shale, fine sandstone, medium sandstone, coarse sandstone, and microconglomerates (if applicable), damage zone, and fault core. Samples from the fault core were composed of cataclasite, crushed breccia, shale gouge, and protocataclasite. Thin sections were cut from the field samples and analyzed under petrographic microscope under cross-polarized view.

Density analysis was performed with a helium pycnometer UltraPyc 1200e (Quantachrome Instruments) on 11 samples from the Macigno and Cilento sites. Samples were first cleaned and then analyzed with a mercury-intrusion PoreMaster 33 porosimeter (Quantachrome Instruments) to measure total porosity and pore size distribution in the range of 0.0064 to 950 μm. Before measurements, samples were dried at 40°C for 24 hr, and then 2 g of material was analyzed in a sample cell of 1.0 × 3.0 cm. The parameters used

Table 1: List of faults studied along with the associate formation, location, and characteristics.

Fault_ID	Location	Kinematics	Orientation	Offset	Fault core	Classification	Type of package
FIE	Boccale, Macigno Fm.	Dip slip (normal)	200°, 65°	0.4 m	Minimal in sandstone, shale gouge through clay	Incipient fault	Evenly thick
FIU	Buca delle fate, Macigno Fm	Oblique (normal, dextral)	211°, 35-56°	0.5 m	Cataclasite, shale gouge	Incipient fault	Unevenly thick
FWE	San Marco di Castellabate, San Mauro Fm.	Oblique (normal, sinistral)	296°, 86°	>30 m	Fault breccia, shale gouge	Well-develop fault	Evenly thick
FWU	Buca delle fate, Macigno Fm	Oblique (normal, sinistral)	256°, 12-51°	1.3 m	Protocataclasite, shale gouge	Well-developed fault	Unevenly thick
FCE	San Marco di Castellabate, San Mauro Fm.	Oblique (normal, sinistral)	304°, 86°	3.5 m	Cataclasite, shale gouge	Complex fault 3 fault planes	Evenly thick
FCU	Sassoscritto, Macigno Fm	Oblique (normal, sinistral)	225°, 80°	2.1 m	Cataclasite, shale gouge	Complex fault 3 fault planes	Unevenly thick

Note: all measurements done in right hand rule.

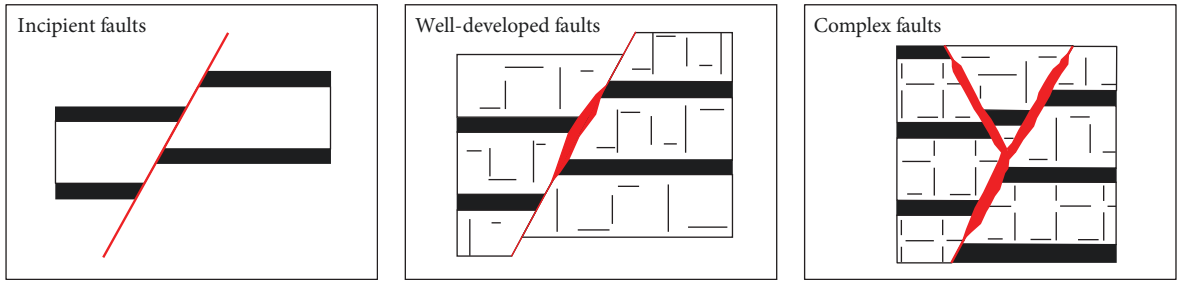

Figure 3: Faults were divided into groups based on the overall architecture. Black layers are representative of claystone, whereas the white beds represent a more competent layer, such as sandstone, limestone, and conglomerates. (a) Incipient faults are usually small in offset (<0.50 m) and are characterized by their lack of fault core; (b) well-developed faults are characterized by the presence of a fault core (in red); (c) complex faults contain two or more fault planes that contribute to an overall more mature fault core.

for porosity measurements are as follows: pressure range, 0.5-33000 psi; contact angle of mercury, 140 degrees; and surface tension of mercury, 0.48 N/m (480 dyn/cm). The obtained mercury intrusion curves approximate pore size distributions, being the applied hydraulic pressure, (P) related to the cross-sectional radius, and (R) of pore throats accessible by the pressured mercury [72].

3.3.2. X-Ray Micro-CT 3D Image Analysis. A total of eleven fault core samples (Table 2) were collected to be investigated using the synchrotron-based X-ray micro-CT imaging technique. In the laboratory, samples were carefully cut into thin cylinders (diameter ~3 mm, length 10-40 mm). The samples were targeted according to the sampling area: (i) Buca delle Fate (BDF_) and (ii) Sassoscritto (SS_). The pores sizes are smaller than 10 microns, and the grains may be characterized by highly variable mineral composition and mass density. In order to obtain an accurate assessment of the pore structure, work was done in phase-contrast mode with a high spatial resolution (ca. 2 microns).

The selected rock samples were scanned at the SYRMEP (SYnchrotron Radiation for MEdical Physics) beamline of Elettra Synchrotron (Trieste, Italy), following the methodology (including image processing and quantitative analysis) described by previous authors [73–75], which is suitable for many types of rocks (e.g., [76–80]). At the SYRMEP beamline, a bending magnetic source is located 23 m from the source, allowing a nearly parallel geometry and a high spatial coherence of the X-ray beam [81, 82], which takes full advantage of phase-contrast effects [83].

For the experiments, a white beam configuration mode [84] was used setting the X-ray energy to 22 keV and filtering the X-ray beam with 1.5 mm Si + 0.025 mm of Mo. The sample-to-detector distance was set at 150 mm and 200 mm. For each sample, 1800 projections were acquired over a total scan angle of 180° with exposure time/projection of 2 s, 2.5 s, or 3.0 s (depending on the sample and the quality output image). The detector consisted of a 16 bit, air-cooled, sCMOS camera (Hamamatsu C11440-22C) with a 2048 × 2048-pixel chip. The effective pixel size of the detector varies from 1.25 μm to 1.80 μm (depending on the sample), yielding a view of approximately 2.5 mm × 2.5 mm.

The tomographic slice reconstruction of the synchrotron X-ray microCT images was performed using the SYRMEP Tomo Project software developed at Elettra [85] and powered by ASTRA tomography toolbox [86] and TomoPy [87]. To improve their liability of quantitative morphological analysis and enhance the contrast among the different mineralogical components of the solid phases and the porous phase, a single-distance phase-retrieval algorithm was applied to the white beam projections using Paganin's algorithm [88] based on the Transport of Intensity Equation (TIE). After reconstruction, 3D images were filtered, segmented, and analyzed using the Pore3D software library, custom-developed at Elettra [89]. A 3D bilateral filter was applied to the reconstructed data for removing noise and preserving edges [90]. Considering the multiphase composition of the imaged rocks, an automatic multiphase k-means clustering [91] with four to five classes was used for segmenting suitable volumes of interests in two phases: (i) pores and (ii) grains (including material with different mineralogy and cement). Permeability is proportional to the square of the porosity and inversely proportional to the square of the specific surface area as in the Kozeny-Carman equation [92, 93]:

$$k = \frac{\phi}{\beta \times \tau^2 \times S_v^2}, \tag{2}$$

where β, the pore shape factor, is fixed to the common value of 5. The tortuosity, τ, defined as the radio of the geodesic length (shortest path connecting two points in the pore space) and the Euclidean length (shortest distance between two points), which generally varies between 1.5 and 2.0 in rocks. However, the permeability should be also controlled by the connectivity, which may vary in function of the cementation degree.

The quantitative analysis consists of measuring the following parameters (sensu [73–75]):

(i) Total porosity, ϕ_t (%): the volume of pores (connected and/or isolated) divided by the total rock volume

Table 2: Volumes of interest analyzed.

Name	Description	Voxel size (μm)	Size in voxels	Volume (mm^3)
BDF_1a	Well-developed fault; sandstone	1.37	$500 \times 500 \times 500$	0.32
BDF_1b	Well-developed fault; sandstone	1.37	$900 \times 900 \times 620$	1.29
BDF_2a	Incipient fault; sandstone	1.37	$1200 \times 1200 \times 620$	2.30
BDF_2b	Incipient fault; sandstone	1.37	$1200 \times 1200 \times 1100$	4.07
BDF_6a	Well-developed fault; silty sand	1.37	$1200 \times 1200 \times 620$	2.30
BDF_6b	Well-developed fault; silty sand	1.37	$1150 \times 1150 \times 620$	2.11
BDF_7a	Complex fault; sandstone	1.37	$1200 \times 1200 \times 620$	2.30
BDF_7b	Complex fault; sandstone	1.37	$1200 \times 1200 \times 620$	2.30
BDF_9a	Well-developed fault; sandstone	1.80	$1200 \times 1200 \times 620$	5.21
BDF_11a	Complex fault; sandstone	1.25	$1200 \times 1200 \times 680$	1.91
BDF_11b	Complex fault; sandstone	1.25	$680 \times 680 \times 680$	0.61
BDF_12a	Complex fault; silty gouge	1.80	$620 \times 620 \times 620$	1.39
BDF_12b	Complex fault; silty gouge	1.80	$620 \times 620 \times 620$	1.39
BDF_12c	Complex fault; silty gouge	1.80	$620 \times 620 \times 620$	1.39
SS_1a	Complex fault; sandstone	1.37	$1200 \times 1200 \times 620$	2.30
SS_1b	Complex fault; sandstone	1.37	$1200 \times 1200 \times 620$	2.30
SS_2a	Complex fault; sandstone	1.80	$620 \times 620 \times 620$	1.39
SS_2b	Complex fault; sandstone	1.80	$620 \times 620 \times 620$	1.39
SS_3a	Complex fault; shale gouge	1.37	$500 \times 500 \times 500$	0.32
SS_3b	Complex fault; shale gouge	1.37	$620 \times 620 \times 620$	0.61

(ii) Specific surface area, S_v (mm^{-1}): the surface of pores divided by the total volume of pores

(iii) Euler characteristic, Eu. Ch. (mm^{-3}): for the purpose of this paper, the Euler characteristic is a connectivity index for the 3D pore network [94]. The value of the Euler characteristic tends to be higher and positive when the number of the pores not connected to each other exceeds the number of connected pores. On the contrary, it tends to be lower and sometimes negative when the connectivity of the pore network increases

4. Results

4.1. Field-Based Permeability Measurements. Average permeability values in the host rock of different lithofacies varied according to values in Table 3. In clay beds, values range from 0.0046 to 0.0433 D. Silt beds and fine sandstone values vary over two orders of magnitude, the former at 0.0101 to 0.864 D and the latter 0.093 to 0.485 D. For the most part, sandstone beds vary over one order of magnitude. Medium sandstone varies from 0.366 to 3.088 D. Coarse sandstone varies from 0.738 to 2.268 D. Permeability values in conglomerates do not vary significantly from 2.085 to 3.088 D. Heterolithic packages derive values ranging from 0.101 to 1.849 D. This variability is most likely from the introduction of sand into the silt beds.

For a better visualization of the relative variation of permeability across the fault zone and the different lithologies, permeability values (normalized by the highest value for each lithofacies) are represented in graphs versus the distance to the fault core and divided per lithofacies (Figures 4–6). The results are also divided by the fault architecture classified as follows: (i) incipient, (ii) well-developed, and (iii) complex faults.

4.1.1. Incipient Faults. In the two analyzed faults, a different behavior of the normalized permeability was observed. In the fault FIE (Figure 4(a)), characterized by a single plane and an evenly thick package distribution, the permeability in the damage zone tends to decrease towards the fault. All the lithofacies show similar results. However, it is less evident for the microconglomeratic facies. Whereas in the fault FIU (Figure 4(b)), characterized by different segments and unevenly thick package distribution, the permeability within the damage zone shows differing trends. In other words, the permeability could increase or decrease towards the fault. This trend seems related to the architecture of the fault, which means that increments of permeability are associated with the presence of linkage zones in the fault segments.

Regarding the fault core in fault FIE, fault core permeability values decrease. In the clay bed, permeability levels ranged from 0.005 to 0.015 D (Figure 4(e)). In coarse sandstone, values are an order to two orders of magnitude greater, spanning from 0.240 to 1.762 D. In the case of fault FIU, fault core permeability values are more variable. In heterolithic successions with a large influence of silt, values range from 0.001 to 0.036 D (Figure 4(f)). In the fault core associated with medium sandstone beds, values are highly variable,

Table 3: Table of average porosity, and pore size of the 7 main facies and 2 faults that produced different types of fault core along the same plane.

Sample	Lithology	Structural domain	Porosity (%)	Pore size (μm)	Average permeability (D)
BDF_1A	Siltstone/medium sandstone	*Host*	14.74	0.087	0.0162
BDF_1B	Siltstone/medium sandstone	*Host*	12.55	0.072	0.2925
BDF_1C	Fine sandstone	*Host*	5.62	0.26	0.0661
SM_A	Fine sandstone w/heavy lithics	*Host*	17.85	0.42	0.145
SM_L	Medium sandstone	*Host*	18.39	0.22	0.1126
SM_D	Medium sandstone	*Host*	8.99	0.21	0.1668
SM_F	Coarse sandstone	*Host*	10.14	1.22	0.0979
SSI_HBC	Fault breccia clast	*Fault*	14.89	0.55	0.0351
SSI_HBV	Vein inside fault breccia	*Mineralized breccia*	10.62	0.28	0.0024
SM1_2S	Shale gouge	*Fault*	4.46	0.033	0.0039
SM1_2	Sandy breccia	*Fault*	4.29	19.48	0.1577

ranging from 0.088 to 2.268 D. Coarse sandstone is relatively high and stable, ranging from 1.531 to 2.468 D.

4.1.2. Well–Developed Faults. When comparing permeability values across well-developed faults in evenly and unevenly thick layers, a stark contrast is apparent (Figures 5(a) and 5(b), respectively). In evenly thick layers, permeability values decrease at the fault core with respect to the damage zone (Figure 5(c)). In unevenly thick layers, permeability values increase (Figure 5(d)). In the fault core, the lowest values are found in the silt layers, from 0.008 D to 0.072 D (Figure 5(e)). In contrast, silt beds with a large percentage of silt (>45%) have up to 2 orders of magnitude larger values, 1.7133 to 4.834 D. The fault core associated with fine sand and coarse sand has about the same values, ranging from 0.642 to 1.408 D (Figures 5(e) and 5(b), respectively).

In evenly thick layers, relative fault core values were lower in respect to unevenly thick layers. In the fault core associated with clay beds, permeability values range from 0.004 to 0.0171 D (Figure 5(e)). In breccia, values remain relatively stable, from 2.085 to 4.705 D. In gouge associated with sand and silt beds, values are intermediate, from 0.157 to 0.955 D.

4.1.3. Complex Faults. Complex faults show a decrease in permeability across fault zones in evenly layered packages and an increase in across fault zones in unevenly thick layers (Figures 6(a) and 6(b), respectively). For faults cutting unevenly distributed layers, the fault core in silt with lithics ranges from 1.713 to 4.838 D, whereas in relatively pure silt, values are much lower at 0.008 to 0.072 D. In fine sand, values span an order of magnitude from 0.641 to 1.408 D (Figure 6(e)). Coarse sandstone is similar at 0.574 to 1.258 D (Figures 6(e) and 6(f), respectively).

In evenly thick packages, permeability values are overall much lower. The largest values are found in gouge associated with sand layers, with values from 0.048 to 1.369 D (Figure 6(f)). Intermediate values are found in gouge associated with heterolithic successions, as values range from 0.0900 to 0.1867 D. The lowest values are found in clay, with values ranging from 0.003 D to 0.017 D.

4.2. Laboratory-Based Porosity and Grain Size Distribution. Pore size ranges from averaged 0.080 μm for siltstones and 0.340 μm for fine sandstones. In medium sandstone, the values are quite different, from 8.99 to 18.39 μm. Coarse sandstone pore size is 10.14 μm. In faulted material, intermediate values are found in crushed breccia (0.55 μm). Pore size is smallest in shale gouge (0.033 μm) and largest in breccias associated with sandstone beds (19.48 μm). Details of the pore size distribution are in Figures 7 and 8.

Porosity values found in the host rock vary, even within the same grain size (Table 3, Figures 7 and 8). In host rock, fine sandstone with a high amount of lithics has a higher value of porosity (17.85%), in relation to relatively "clean" fine sandstone (5.62%). The porosity of medium sandstone beds varies greatly, from 18.39% to 8.99%. Coarse sandstone beds have a relatively intermediate porosity of 10.14%. In the fault core, fault breccias have the highest amount of porosity (14.89%) whereas the gouges had relatively similar values (4.46% and 4.29%).

4.3. Microstructural and Mineralogical Analysis of Host Rock. Thin section analysis revealed microstructures and mineralogy of sampled lithologies present (Figure 9). Claystones exhibit weak to moderate iso-orientation to bedding (Figure 9(a)) and are composed mainly of quartz and feldspar crystals and/or mica grains. Siltstone facies are generally moderately sorted, subangular to subrounded (Figure 9(b)). They are composed of a mosaic of very closely packed quartz and feldspar detrital grains and authigenic crystals. White mica is common. Brownish to gray limonite groundmass fills the intercrystalline space and occurs as sparse nodules and as rust red or brownish impregnations/coatings on quartz and feldspar crystals. Numerous tiny limonite veins occur as well, surrounded by limonite halos that fill the host rock. Thin sections taken from fine sandstone consist mostly of detrital quartz (Figure 9(c)). Grains are generally subangular to subrounded and closely packed. Sorting is moderate. Several white mica flakes occur, and their iso-orientation forms a subtle layering. Brownish limonite groundmass fills the intergranular space. Medium sandstones in the studied areas

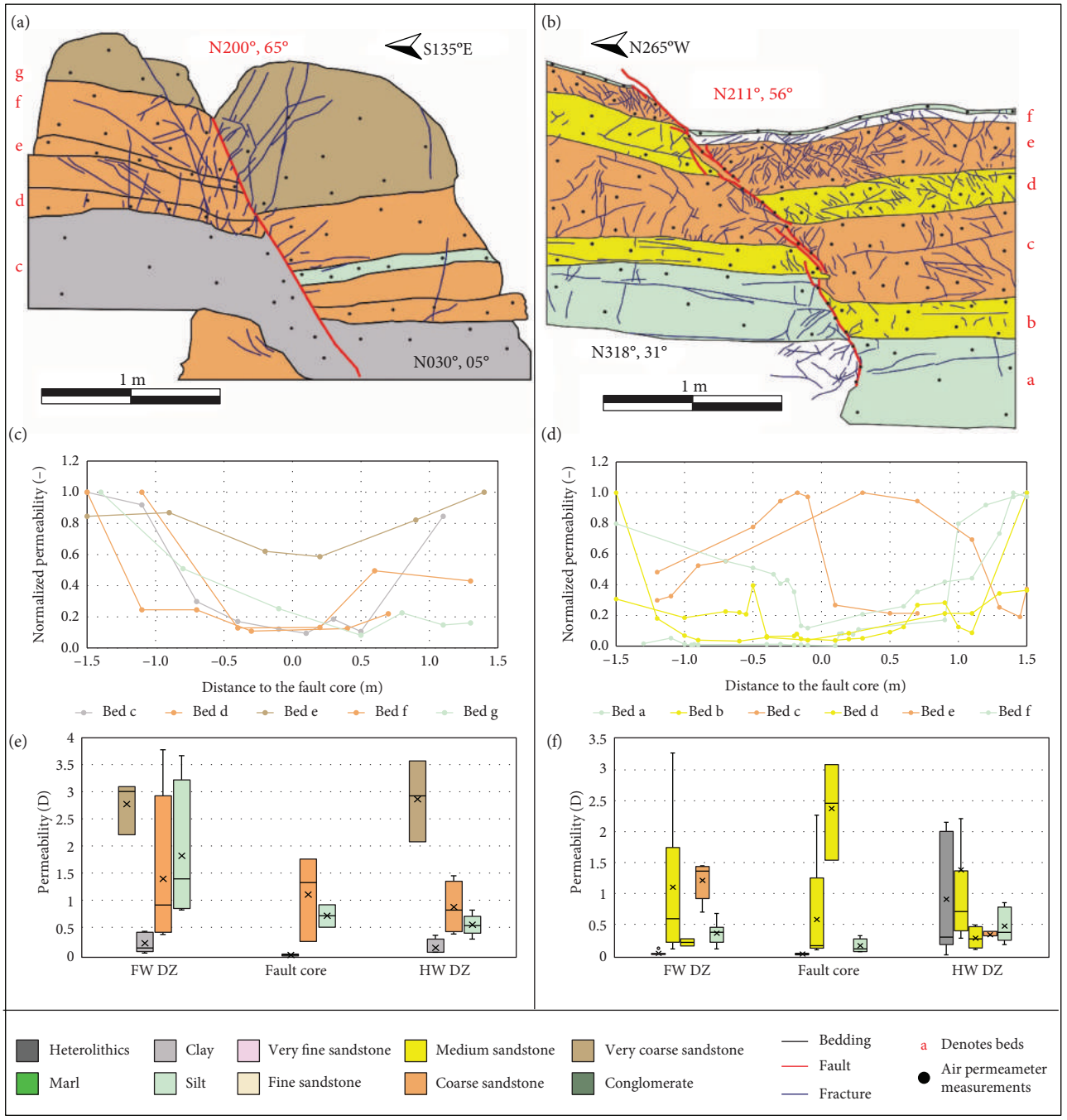

FIGURE 4: Permeability across incipient faults in different styles of multilayer package. Fault orientation is denoted in right hand rule with red text, whereas bed orientation is in black text: line drawings (a) of the FIE fault, which cuts through packages of evenly distributed clay layers and (b) the FIU fault, which cuts through packages with unevenly distributed clay layers. Fault orientation is denoted in right hand rule with red text, whereas bed orientation is in black text; permeability normalized for bed thickness for the (c) FIE fault and (d) FIU fault; variation of permeability measurements shown in a box and whisker plot, in order to show the high variability across the damage zone in the hanging wall (HW DZ), the fault core, and the damage zone of the footwall (FW DZ) in (e) the FIE fault and (f) the FIU fault. Color meaning is denoted in the legend below.

consist mostly of detrital quartz (generally monocrystalline), and feldspars (K-feldspars and plagioclase), as well as authigenic minor white mica (Figure 9(d)). Grains are subangular to subrounded and closely packed. Sorting is poor to moderate. Brownish limonite groundmass fills the intergranular space. Coarse-grained sandstones consist of detrital quartz (both mono- and polycrystalline), feldspars, and rock fragments (Figure 9(e)). Conglomerate grains are subangular and closely packed with a poor sorting (Figure 9(f)). Brownish limonite groundmass fills the intergranular space. Grains

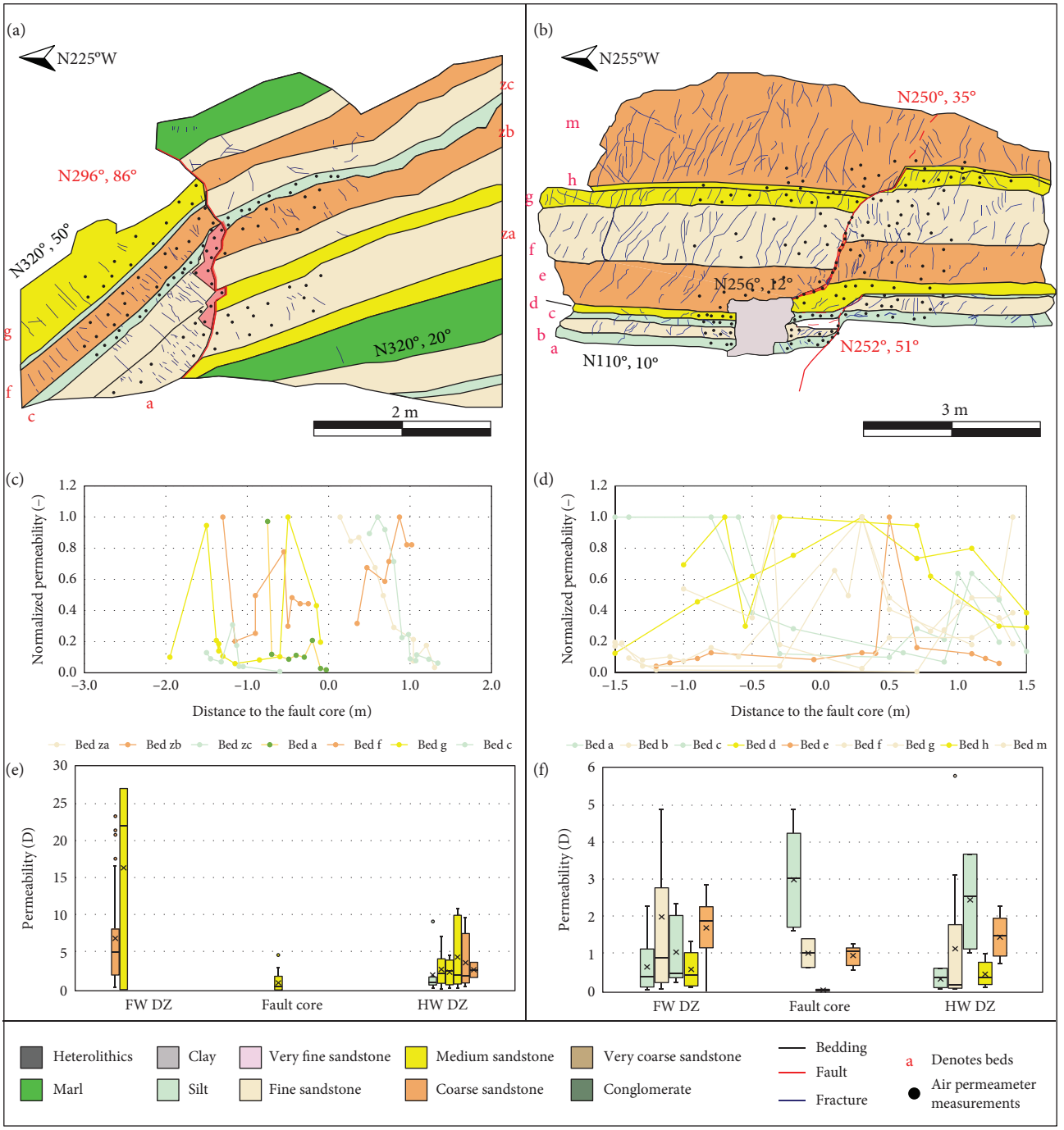

FIGURE 5: Permeability across well-developed faults in different styles of multilayer package. Fault orientation is denoted in right hand rule with red text, whereas bed orientation is in black text: line drawings of (a) the FWE fault, which cuts through packages of evenly distributed clay layers, and (b) the FWU fault, which cuts through packages with unevenly distributed clay layers. The grey block is representative of travertine deposit that covers the outcrop; permeability normalized for bed thickness for (c) the FWE fault and (d) the FWU fault; variation of permeability measurements shown in a box and whisker plot, in order to show the high variability across the damage zone in the hanging wall (HW DZ), the fault core, and the damage zone of the footwall (FW DZ) in (e) the FWE fault and (f) the FWU fault. Color meaning is denoted in the legend below.

consist of detrital quartz (both mono- and polycrystalline), feldspars, and rock fragments (mostly quartz-feldspar crystalline rocks), as well as authigenic rare white mica. Except for mica flakes, grains are subangular and closely packed, and overall sorting is poor. There is evidence of intergranular pressure solution (microstylolites) on boundaries of some quartz grains. Brownish limonite groundmass fills the intergranular space.

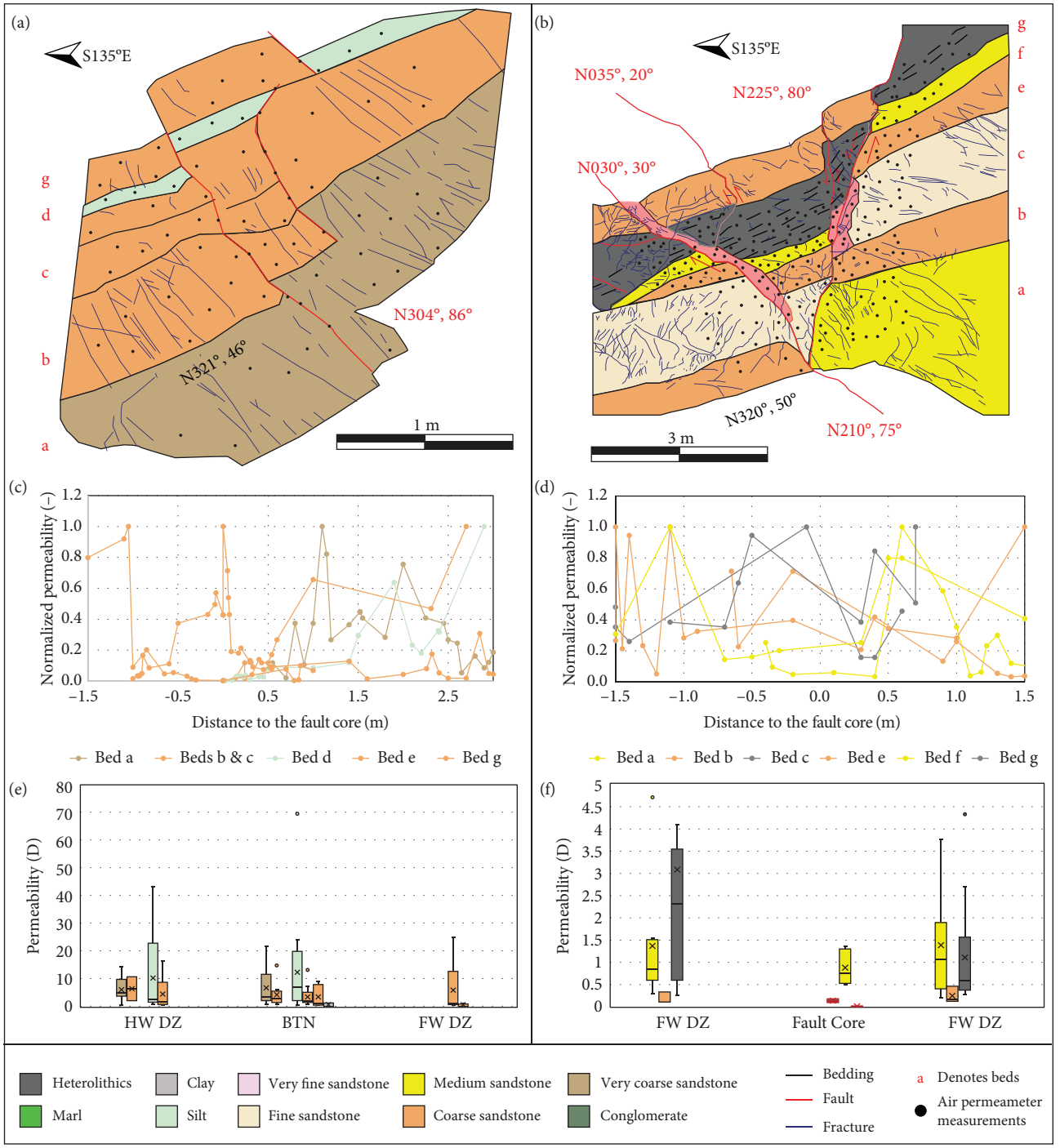

Figure 6: Permeability across complex faults in different styles of multilayer package. Fault orientation is denoted in right hand rule with red text, whereas bed orientation is in black text: line drawings of (a) the FCE faults, which cut through packages of evenly distributed clay layers, and (b) the FCU faults, which cut through packages with unevenly distributed clay layers; permeability normalized for bed thickness for (c) the FCE fault and (d) the FCU fault; variation of permeability measurements shown in a box and whisker plot, in order to show the high variability across the damage zone in the hanging wall (HW DZ), the fault core between the faults (BTN), and the damage zone of the footwall (FW DZ) in (e) the FCE fault and (f) the FCU fault. Color meaning is denoted in the legend below.

4.4. Microstructural and Mineralogical Analysis of Fault Rock. Thin section analysis of the fault core made up of shale gouge shows a clear initiation of smear along a microfault (offset < 1 cm) (Figure 10(a)). There is also evidence of shale injection around the matrix surrounding coarser-grained material. In thin section analysis of crushed breccia, the boundaries between breccia clasts and interstitial limonite are quite sharp (Figure 10(b)). The angular clasts of

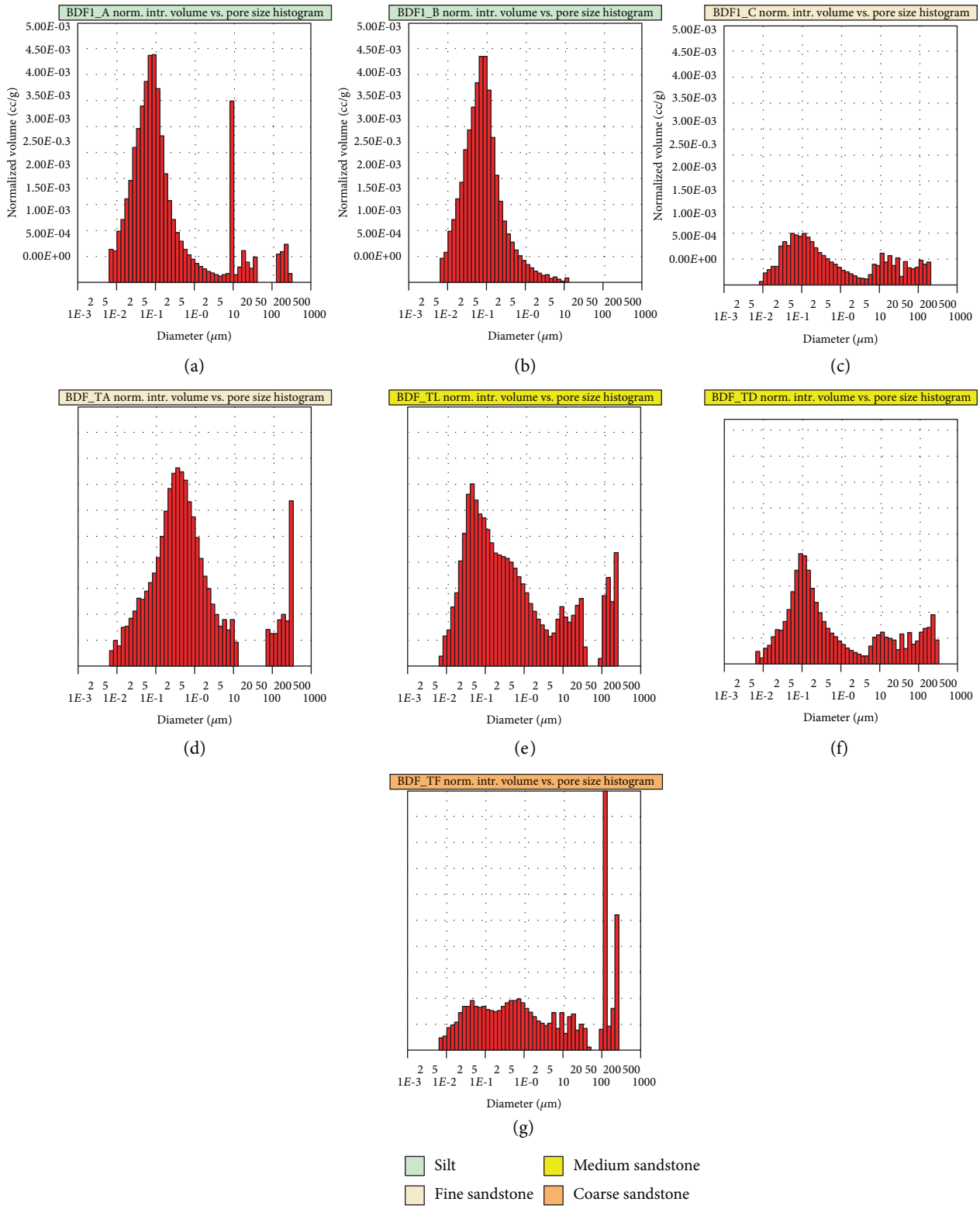

Figure 7: Results of Hg-intrusion pore size distribution analysis of host rock. Color in title denotes grain size.

sandstone are made of closely packed grains with intergranular limonite, which also coats/impregnates some grains. Calcite crystals are coarse, from bladed at the patch boundaries to equant in the patch center, indicating the progressive filling of preexisting large voids suddenly created by the brecciation. Calcite crystals were later partly dissolved with formation of small equant vuggy pores.

In cataclasites, there are several samples with parent rock of differing material, which show different characteristics (Figures 10(c)–10(e)). In cataclasite stemming from

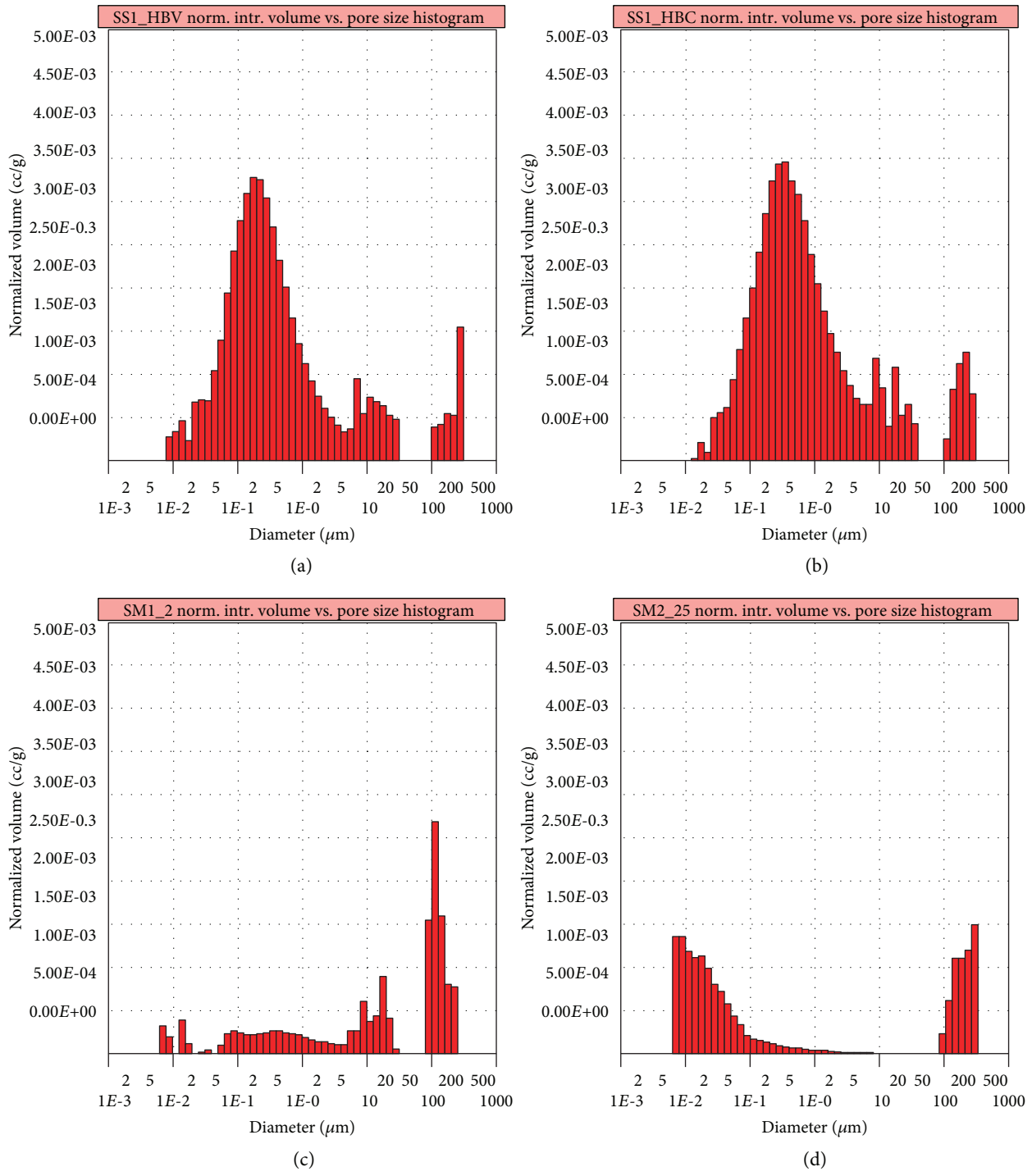

Figure 8: Results of Hg-intrusion pore size distribution analysis of fault rock.

heterolithic beds, cataclasite clasts can be distinguished by sharp changes in grain iso-orientation and zones richer in limonite between probable clasts. The rock is rich in white mica that is not iso-oriented parallel to the fault. Mica is mixed with both quartz and feldspar detrital grains (irregular "eroded" geometries and microfractures) and authigenic crystals of feldspar (euhedral, "rectangular shapes") and quartz.

In cataclasites originating from sandstone, it is possible to distinguish sandstone clasts from interstitial sandstone (cataclasite matrix) (Figure 10(d)). Sandstone clasts are made of closely packed grains of detrital quartz (both poly- and monocrystalline) and feldspars, crystalline rock fragments, and rare mica flakes. The matrix also includes some grains made of limonite with floating detrital quartz and feldspar, suggesting multiple episodes of cataclasis and fault rock

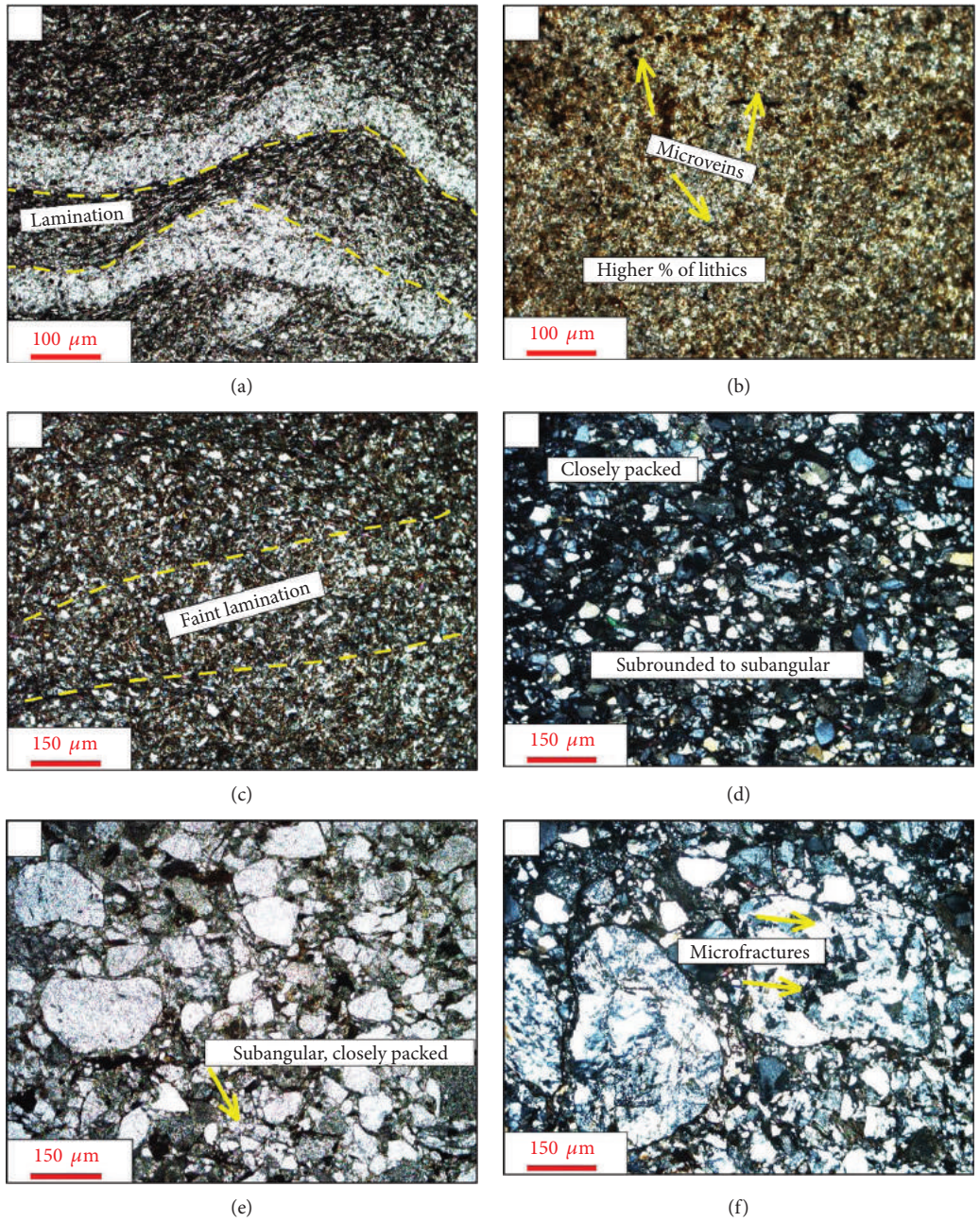

Figure 9: Thin sections of host rock found in the study area examples from: (a) claystone exhibiting plastic flow; fine sand: (b) siltstone with microfractures present; (c) fine sand with subtle layering iso-oriented; (d) medium sandstone; (e) coarse sandstone; (f) conglomerate.

mineralization. In another sample taken from a different cataclasite fault core, sandstone clasts made of closely packed grains are surrounded by interstitial sandstone made of relatively loosely packed grains of detrital quartz and feldspar with more intergranular brownish to rust red limonite than sandstone clasts (Figure 10(e)). In foliated cataclasite, loosely packed detrital quartz and feldspar grains are iso-oriented parallel to the fault and intergranular limonite is recognizable in the probable cataclasite matrix, although cataclasite clasts are not recognizable (Figure 10(f)). Large patches of dark brown to rust red limonite, mixed with later limpid equant calcite (mottled limonite/calcite texture), are present in the probable cataclasite matrix, as well as small limonite veins.

4.5. X-Ray MicroCT 3D Descriptive and Quantitative Analysis of Pore Network. Synchrotron samples yield further insight into the microstructures developed within the fault core. The rock within the fault core can be highly variable due to the fact that they derive from different lithofacies and diagenesis processes (Table 4, Figures 11 and 12).

In order to evaluate the effect of both textural properties (Kozeny-Carman equation) and connectivity (Euler characteristic), both results have been plotted in a scatter graph

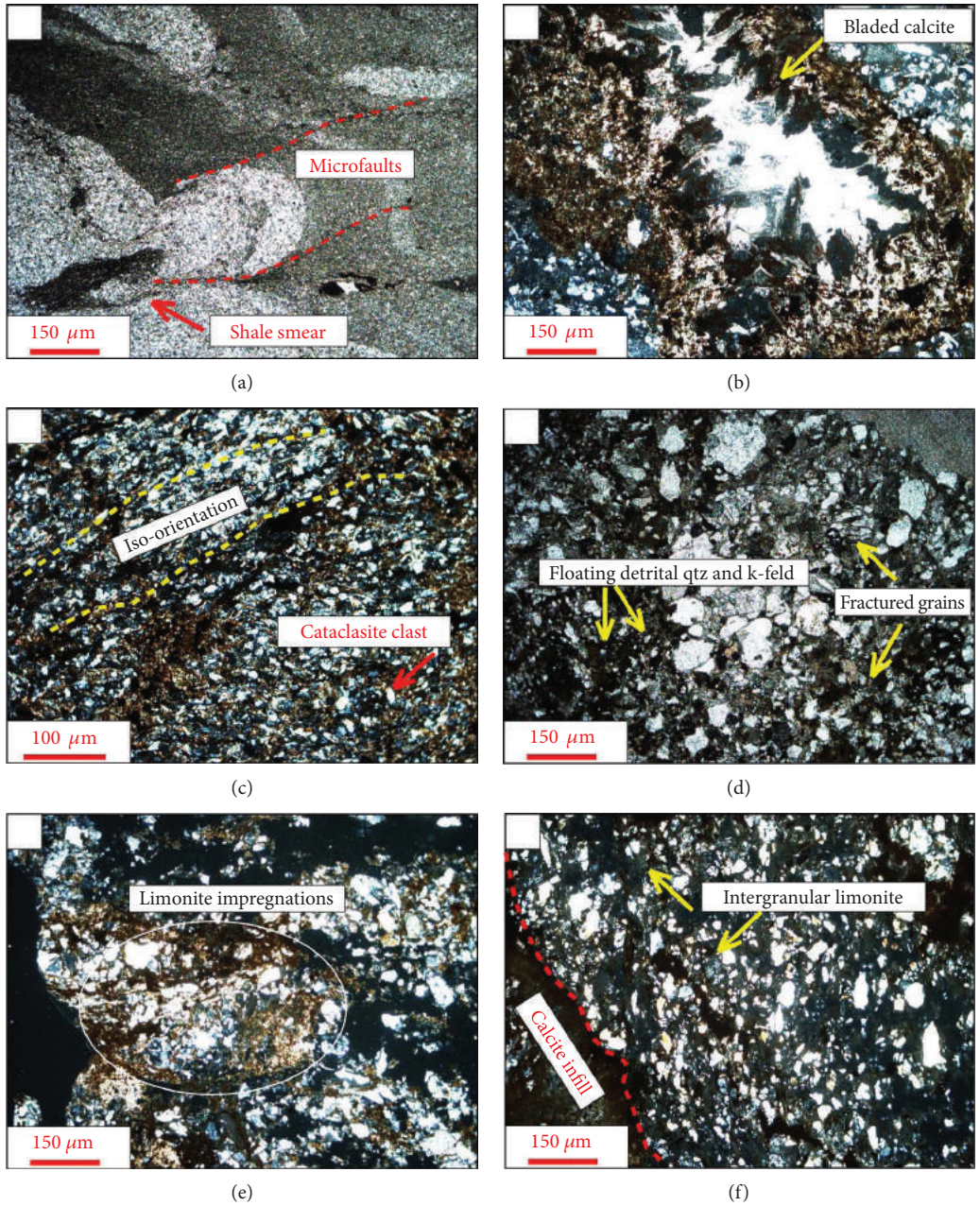

Figure 10: Thin sections cut from samples of fault core. (a) The darker parts are dominated by mica flakes and clay. Mica flakes have a tendency to iso-orientation and evidencing plastic flow within the lighter parts, which are made mainly of quartz and feldspar crystals and/or grains; (b) interstitial limonite between breccia clasts is rust red to dark brown (mottled color changes) and includes rare host rock-derived grains and patches of later calcite crystals in the middle of breccia clast interspaces; (c) cataclasite grains are barely distinguishable, both grains and crystals are fine sand to silt in size, and the interstitial spaces are filled by limonite that also coats/impregnates some grains and crystals; (d) interstitial sandstone is made of relatively loosely packed grains (detrital quartz and minor detrital feldspar, rock fragments, and mica) with more intergranular brownish to rust red limonite (also coating/impregnating some grains) than sandstone clasts; (e) fractured grains found in both clasts and matrix of the cataclasite; (f) grains iso-oriented parallel to the fault and with intergranular limonite are recognizable in the probable cataclasite matrix.

(Figure 11). In this graph, pervious rock samples, characterized by a higher porosity, wider pores (lower specific surface area), and better connectivity (lower Euler characteristic), are localized to the upper left area. Rock samples located to the right of the graph tend to have a poorly connected pore network (more impervious).

Sand-rich fault cores highly affected by dissolution tend to have the highest values of porosity, lowest of specific surface area, and lower Euler Characteristic (BDF_2a and SS_1a/b, Figures 12(a), 12(e), and 13(a)). Cementation is also present in some fault cores (Figure 12(d)), which drastically reduces the connectivity of the pore network. In the case of

Table 4: Results X-ray microCT 3D analysis of the pore network.

Name	ϕ_t (%)	S_v (mm^{-1})	Eu. ch. (mm^{-3})
BDF_1a	4.6	380.4	16003.4
BDF_1b	3.0	306.7	6532.2
BDF_2a	8.3	236.1	3831.9
BDF_2b	0.8	475.0	6486.8
BDF_6a	4.9	302.0	8823.6
BDF_6b	5.0	348.0	6988.5
BDF_7a	1.2	583.3	15308.2
BDF_7b	2.6	507.7	17519.1
BDF_9a	1.8	366.7	8067.4
BDF_11a	0.5	320.0	2502.4
BDF_11b	0.8	375.0	8797.2
BDF_12a	0.3	533.3	3679.1
BDF_12b	2.7	377.8	9949.3
BDF_12c	1.6	431.3	11936.7
SS_1a	8.7	287.4	2967.4
SS_1b	8.1	298.8	3953.8
SS_2a	2.2	381.8	10465.5
SS_2b	0.3	466.7	2181.9
SS_3a	1.9	431.6	13853.1
SS_3b	1.9	468.4	19135.4

Notes: ϕ_t: total porosity; S_v: specific surface area; Eu. Ch.: Euler characteristic.

silt- and clay-rich fault cores (Figures 12(f) and 13(b)), they are characterized by low porosity and very high values of Euler characteristics and specific surface area, indicating a pore network composed by isolated small pores (Figure 11).

In the samples from the Buca delle Fate (BDF) area, it was common to identify some microfractures. Protocataclasite material, characterized by microporosity, is also common and occasionally significant within the sample. Microfractures occasionally connect cataclastic zones. Samples BDF_1a and BDF_1b are characterized by a poorly connected pore network. Microfractures are present along with lithic material, like pyrites and mica. There are also microporosity areas related to diagenesis or protocataclasis. Sample BDF_2a has similar characteristics to BDF_1a and BDF_1b, but also contains evidence of a left-over vein after grain dissolution (Figure 12(a)). Some fractures present mineral precipitations connecting the opposite walls which validates the hypothesis of natural origin for most of the observed micro fractures. Sample BDF_2b is characterized by the presence of microfractures. There are some mineral growths within them, which can influence porosity. In some samples (BDF_6a and BDF_6b), possible shearing bands characterized by a higher porosity and connectivity (visually) were identified (Figure 12(b)). Some volumes characterized by microporosity are likely dissolution-related pore space. Samples BDF_7a and BDF_7b are characterized by grain size reduction. Most samples contain microfractures of varying intensity, along with grain size reduction and cataclasis (Figure 12(c)). A few samples show a high content of fine-grained material associated with cataclasis. Within the volumes, dissolution of calcite also took place generating pores that are shaped like bladed calcite (sample BDF_9a) (Figure 12(d)). Some minerals like pyrites and/or other oxides are present within the samples. Sample BDF_11a, BDF_11b, and BDF_12a contain multiple microfractures with grain dissolution and minerals growing within the fractures, where oxidation is also present.

In the Sassoscritto (SS) samples, there are three prominent different textures and characteristics: (i) Samples SS_1a and SS_1b show well-defined grains and intergranular pore space, rare pore dissolution, and pyrites/oxides. Some grains present visible fractures (Figure 12(e)). (ii) Samples SS_2a and SS_2b show porous grains in sharp contact with clay material. (iii) Samples SS_3a and SS_3b are entirely composed of clay material (clay smeared material), characterized by isolated porosity (Figure 12(f)). Colored bands are present, possibly related to mineral alienation due to deformation.

5. Discussion

5.1. Permeability in the Damage Zone. The permeability in the damage zone may decrease or increase towards the main fault surface. This is likely due to the presence of microfractures, which is evidenced in thin section and synchrotron analysis. If microfractures are healed/sealed, matrix permeability decreases. These healed/sealed microfractures have been evidenced in thin sections, where microfractures may be filled by calcite and/or limonite. In some places, the limonite veins cut through calcite. There are also limonite halos in the intergranular space surrounding veins, with higher concentrations towards the vein as opposed to away from it, determined by the change in color from a dark red to light.

If microfractures are open, the matrix permeability may increase. This cannot be interpreted as a recent activity of the fault after exhumation as it is not general behavior and is normally associated with linkage areas. Therefore, it is interpreted that in certain areas of the fault zone, the differential stress allows the "recent" formation or opening of microfractures. Therefore, the cementation has not completely occluded the microfractures pore space. Fault architecture plays an important role in the distribution of these areas with higher matrix permeability. In an uneven distribution of the relative thickness, faults are normally composed by various segments and therefore more linkage areas. Of course, this behavior may vanish after the fault segments become totally connected. In the case of evenly thick packages, fault architecture is mainly characterized by a through-going plane; therefore, the permeability tends to decrease towards the main fault surface due to cementation.

5.2. Permeability in the Fault Core. While the composition of the fault cores in the study area can be highly variable, they are generally very immature and can be classified as protocataclasite. Therefore, the rocks within the fault core are highly related to the surrounding host rock in terms of composition, grain size, and hydraulic properties. Although clay smear is of common occurrence, sand size fault rock also occurs. In

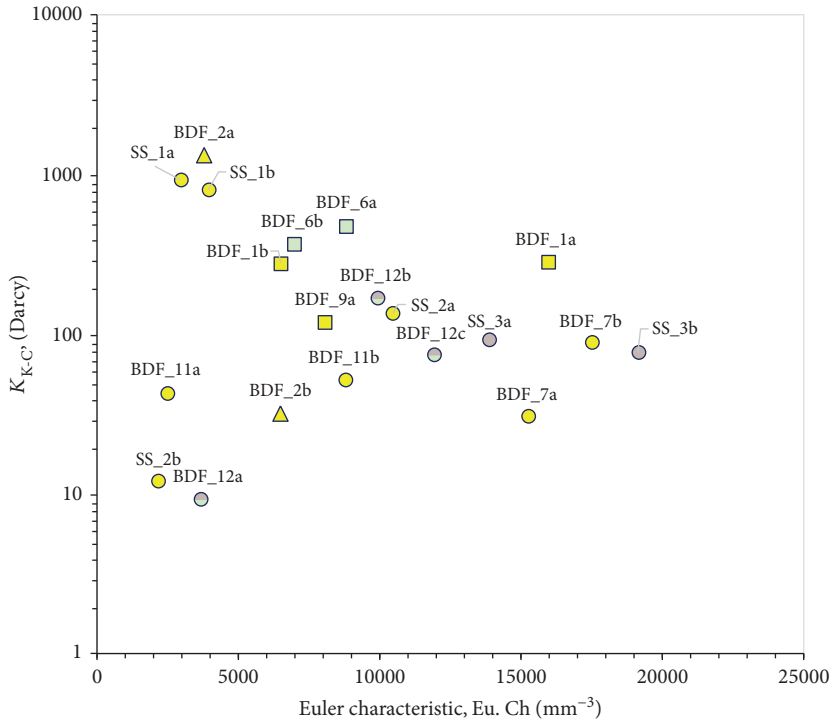

Figure 11: Scatter plot indicating the permeability estimates with the Kozeny-Carman equation ($k_{K\text{-}C}$) versus the Euler characteristic. For the Kozeny-Carman equation [92, 93], it was assumed that both the tortuosity (equal 1.5) and pore shape factor (equal 5) are constant. Rock samples with a higher permeability, wider pores, and better connectivity (more pervious) are localized to the upper left area. Rock samples located to the right of the graph tend to have a poorly connected pore network (more impervious). Description of the samples is located in Table 2. Detailed results in Table 4. Samples in bold can be observed in Figure 12.

general, sediments rich in clay are smeared roughly parallel to the fault plane, whereas sand sediments are deformed into blocks and patches. In consequence, fault core is variable in terms of porosity and permeability.

At the microscale, grain crushing, if present, might lead to an increment of the specific surface area and therefore a decrease in permeability [79]. However, the presence of microfractures may locally enhance the connectivity of the pore space and permeability. In general, samples are characterized by low connectivity (high values of Euler characteristic) due to a high degree of cementation (Figure 12(d)). However, it is expected that some micropores below the resolution of the images can connect the pore space and exert some minor contribution to permeability [79]. Clay-rich fault cores are less connected (highest values of Euler characteristic) and therefore less pervasive. Some samples (BDF_2a and SS_1a/b; Figures 12(a) and 12(e)) are characterized by an important dissolution that increases the porosity and reduces the specific surface area explaining some local enhancement of permeability.

Unevenly thick heterolithic beds, in general, have a relative increase of permeability at the fault core while those evenly thick show a decrease in permeability. This is likely due to the increased repetition of clay or silty clay layers. As more clay is introduced into the fault core, permeability decreases [11, 17, 95]. In evenly thick layers, permeability at the fault core was up to four orders of magnitude lower than permeability in the damage zone. In general, faults that cut through clay layers with displacements larger than 4 m could experience a relative increase in permeability as smear continuity is lost, but in evenly thick layers of heterolithics, the influx of clay material "feeds" the smear and keeps permeability low [17, 96]. This factor is independent of fault offset, as faults with offsets lower than 2 m and as big as 30 m have the same results.

5.3. Consequences to Fault Sealing. In a fault zone, the damage zone is considered generally more permeable than the fault core due to the presence of fractures and fine-grained material, respectively. These interconnected fractures present in the damage zone facilitate fluid migration and storage and can also help the cementation process. The results of this study indicate that matrix permeability can decrease towards the main fault surface despite the expected increment of microfracture density. This may be attributed to the cementation of the microfractures near the once more permeable zone of the fault. Macrofractures observed in the outcrop were also cemented. Cementation may occur from different sources, as different kinds of cement (quartz, calcite, and limonite) are observed in the veins. Fault linkage zones can be characterized by a higher permeability possibly due to the presence of not cemented microfractures. These microfractures can be generated locally at low stress rates right after the last cementation event.

The fault core is shown to be variable in terms of the grain size of the fault rock and its thickness. Both elements

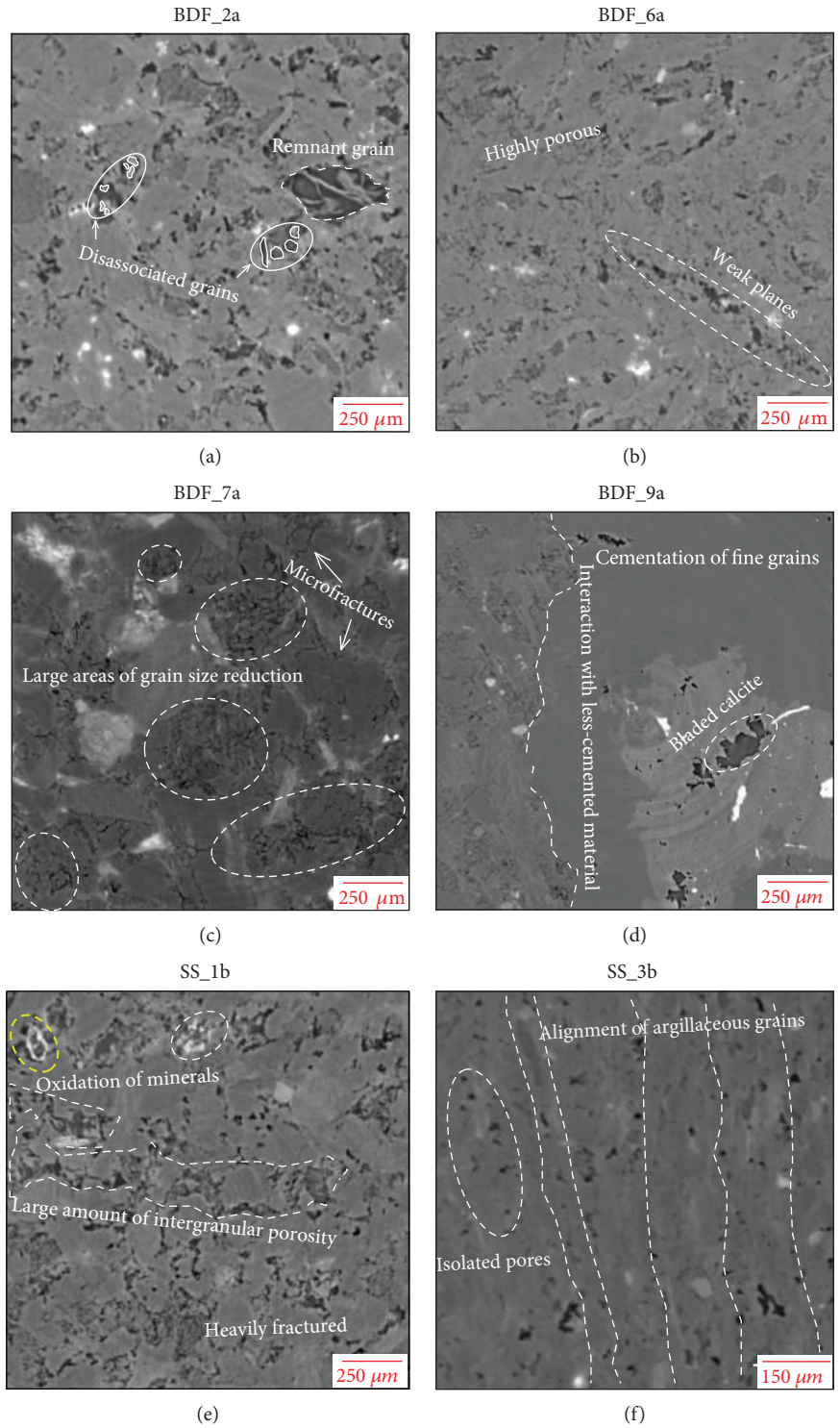

Figure 12: X-ray microCT images of some analyzed fault cores: (a) BDF_2a, sand-rich and affected by dissolution, (b) BDF_6a; silty sand fault core affected by both microfracturing and dissolution, (c) BDF_7a; sand-rich affected both microfracturing and dissolution, (d) BDF_9a; highly cemented sample, (e) SS_1b; sand-rich fault core highly affected by dissolution and microfracturing, and (f) SS_3b; clay-rich fault core with evidence of grain alignment. Description of the samples in Table 2.

have a significant impact on the final hydraulic behavior of the fault. The clay smear is perhaps the most important source of permeability reduction in the studied faults. The fine material in the smear is likely fed from the adjacent shales and siltstones that form from the cataclasis process itself. These fault cores are composed sometimes entirely of lithic blocks of sandstones, which preserve or increase the original permeability. The sealing capacity of the faults

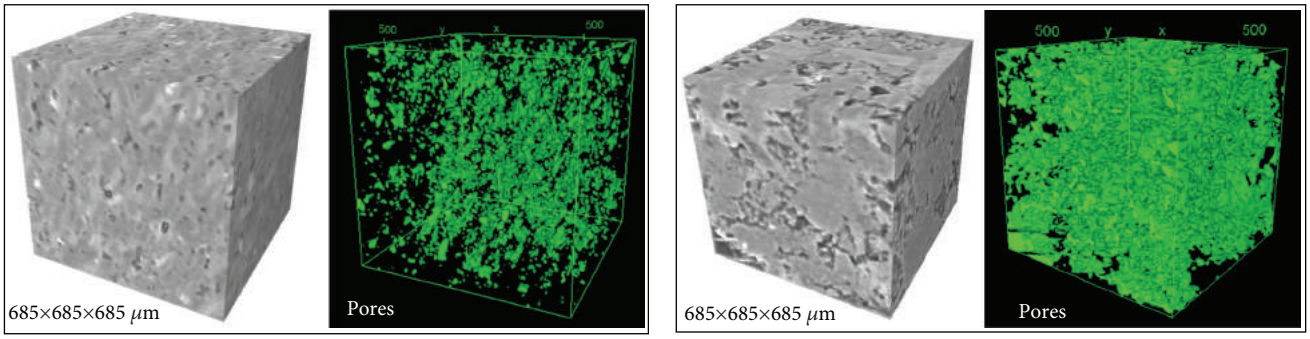

Figure 13: X-ray microCT 3D images of the main types of fault cores found in the study areas: (a) sand-rich fault core and (b) clay-rich fault core (characterized by clay smearing). The samples come from the same fault, which is located at the Sassoscritto area. The grey images correspond to the rendering of the 3D X-ray microCT images, whereas the green volumes to the right are the segmented pore space.

depends on whether the clay-rich fault core is present and the thickness of the fault core.

Although it is suggested that the width of the fault core is related to offset, at faults in the studied area, the fault core width was more associated with lithology [97, 98]. A change in the width of the fault core is usually accommodated for in the damage zone [99]; however, in faults studied at these locations, this is not necessarily true. Faults that passed through adjacent sandstone beds rarely exceeded a fault core width greater than 3 cm, regardless of offset and distribution of beds (evenly or unevenly thick beds). Faults that passed through heterolithic beds adjacent to sandstone created thicker fault cores, from 3 cm to 5 cm wide. Faults that passed through adjacent clay beds produced the widest fault cores, sometimes spanning up to 40 cm. At the studied sites, host rock competency influenced fault core width more than overall offset.

Considering all the elements, the faults with an ideal seal behavior (at least to the studied scale) correspond to faults within an evenly thick layer distribution. These faults are characterized by a clay-rich fault core and a cemented matrix near the main fault surface, which may guarantee a thick, low-permeability barrier zone. The fault with the worst sealing capacity corresponds to small-medium displacement hosted in unevenly thick layers. These faults present important linkage zones for fault segments characterized by relatively high permeability. Moreover, the existence of poorly deformed lithic block embeds in the fault core reduces its sealing efficiency.

6. Conclusions

In this paper, the sedimentological, stratigraphic, and structural controls on matrix permeability in a fault zone were analyzed. This study contributes to the better understanding of the petrophysical behaviors of natural reservoirs and how stratigraphic, sedimentological, and structural discontinuities in the rock may impact fluid flow across fault zones in different types of siliciclastic heterolithic packages.

In the studied faults, the damage zone is characterized by high cementation generally occluding both macrofractures and microfractures (filled with quartz or calcite). The latter revealed a decrease in matrix permeability towards the main fault surface. In this case, a sort of cemented zone around the main fault surface may represent an important barrier for fluid flow. However, linkage zones, generally present in unevenly thick layers, may represent some increment of permeability in the matrix. This may be related to the presence of open microfractures in these zones.

Fault core permeability is mostly related to the rock feeding it. A higher amount of clay layers in evenly thick heterolithic packages increases the amount of clay material in the fault core, effectively lowering permeability. When the layers are evenly distributed, the clay particles feed the already present clay smear, extending its unbroken plane and creating a barrier to fluid flow. In unevenly thick packages, clay smear may still be present, but its connectivity is greatly decreased due to the larger influence of sand particles than clay. In unevenly thick layers, the damage zone remained the less efficient barrier to fluid flow. It is evident that the amount of clay layers and their distribution affect fluid flow across the fault, regardless of fault offset.

Data Availability

The data used to support the findings of this study are available from the corresponding author upon request.

Conflicts of Interest

The authors declare that they have no conflicts of interest.

Acknowledgments

This research was supported by the Reservoir Characterization Project (http://www.rechproject.com) and funded by Neptune Energy, Shell Italia E&P, and Total Italia E&P.

References

[1] R. G. Walker, "Deep-water sandstone facies and ancient submarine fans: models for exploration for stratigraphic traps," *AAPG Bulletin*, vol. 62, no. 6, pp. 932–966, 1978.

[2] L. Zhang, M. Pan, and H. Wang, "Deepwater turbidite lobe deposits: a review of the research frontiers," *Acta Geologica Sinica - English Edition*, vol. 91, no. 1, pp. 283–300, 2017.

[3] P. Dromgoole, M. Bowman, A. Leonard, P. Weimer, and R. M. Slatt, "Developing and managing turbidite reservoirs – case histories and experiences: results of the 1998 EAGE/AAPG research conference," *Petroleum Geoscience*, vol. 6, no. 2, pp. 97–105, 2000.

[4] M. Gainski, A. G. MacGregor, P. J. Freeman, and H. F. Nieuwland, "Turbidite reservoir compartmentalization and well targeting with 4D seismic and production data: Schiehallion Field, UK," *Geological Society, London, Special Publications*, vol. 347, no. 1, pp. 89–102, 2010.

[5] R. H. Sibson, "Fault rocks and fault mechanisms," *Journal of the Geological Society*, vol. 133, no. 3, pp. 191–213, 1977.

[6] R. J. Knipe, "Faulting processes and fault seal," in *Structural and Tectonic Modeling and its Application to Petroleum Geology*, R. M. Larsen, B. T. Larsen, H. Brekke, and E. Talleraas, Eds., pp. 325–342, Norwegian Petroleum Society Special Publications, 1992.

[7] J. S. Caine, J. P. Evans, and C. B. Forster, "Fault zone architecture and permeability structure," *Geology*, vol. 24, no. 11, pp. 1025–1028, 1996.

[8] C. Childs, T. Manzocchi, J. J. Walsh, C. G. Bonson, A. Nicol, and M. P. J. Schopfer, "A geometric model of fault zone and fault rock thickness variations," *Journal of Structural Geology*, vol. 31, no. 2, pp. 117–127, 2009.

[9] D. R. Faulkner, C. A. L. Jackson, R. J. Lunn et al., "A review of recent developments concerning the structure, mechanics and fluid flow properties of fault zones," *Journal of Structural Geology*, vol. 32, no. 11, pp. 1557–1575, 2010.

[10] Y. Pei, D. A. Paton, R. J. Knipe, and K. Wu, "A review of fault sealing behaviour and its evaluation in siliciclastic rocks," *Earth-Science Reviews*, vol. 150, pp. 121–138, 2015.

[11] G. Yielding, P. Bretan, and B. Freeman, "Fault seal calibration: a brief review," *Geological Society, London, Special Publications*, vol. 347, no. 1, pp. 243–255, 2010.

[12] M. Antonellini and A. Aydin, "Effect of faulting on fluid flow in porous sandstones: petrophysical properties," *AAPG Bulletin*, vol. 78, pp. 355–377, 1994.

[13] A. Aydin, "Fractures, faults, and hydrocarbon entrapment, migration and flow," *Marine and Petroleum Geology*, vol. 17, no. 7, pp. 797–814, 2000.

[14] R. G. Gibson, "Fault-zone seals in siliciclastic strata of the Columbus Basin, offshore Trinidad," *American Association of Petroleum Geologists Bulletin*, vol. 78, pp. 1372–1385, 1994.

[15] J. R. Fulljames, L. J. J. Zijerveld, and R. C. M. W. Franssen, "Fault seal processes: systematic analysis of fault seals over geological and production time scales," *Norwegian Petroleum Society Special Publications*, vol. 7, pp. 51–59, 1997.

[16] J. Schmatz, P. J. Vrolijk, and J. L. Urai, "Clay smear in normal fault zones – the effect of multilayers and clay cementation in water-saturated model experiments," *Journal of Structural Geology*, vol. 32, no. 11, pp. 1834–1849, 2010.

[17] P. J. Vrolijk, J. L. Urai, and M. Kettermann, "Clay smear: review of mechanisms and applications," *Journal of Structural Geology*, vol. 86, pp. 95–152, 2016.

[18] K. Corbett, M. Friedman, and J. Spang, "Fracture development and mechanical stratigraphy of Austin Chalk, Texas," *AAPG Bulletin*, vol. 71, pp. 17–28, 1987.

[19] M. R. Gross, M. P. Fischer, T. Engelder, and R. J. Greenfield, "Factors controlling joint spacing in interbedded sedimentary rocks: integrating numerical models with field observations from the Monterey Formation, USA," *Geological Society, London, Special Publications*, vol. 92, no. 1, pp. 215–233, 1995.

[20] W. Narr and J. Suppe, "Joint spacing in sedimentary rocks," *Journal of Structural Geology*, vol. 13, no. 9, pp. 1037–1048, 1991.

[21] J. R. Shackleton, M. L. Cooke, and A. J. Sussman, "Evidence for temporally changing mechanical stratigraphy and effects on joint-network architecture," *Geology*, vol. 33, no. 2, pp. 101–104, 2005.

[22] G. Strijker, G. Bertotti, and S. M. Luthi, "Multi-scale fracture network analysis from an outcrop analogue: a case study from the Cambro-Ordovician clastic succession in Petra, Jordan," *Marine and Petroleum Geology*, vol. 38, no. 1, pp. 104–116, 2012.

[23] S. Tavani, F. Storti, F. Salvini, and C. Toscano, "Stratigraphic versus structural control on the deformation pattern associated with the evolution of the Mt. Catria anticline, Italy," *Journal of Structural Geology*, vol. 30, no. 5, pp. 664–681, 2008.

[24] T. M. Mitchell and D. R. Faulkner, "The nature and origin of off-fault damage surrounding strike-slip fault zones with a wide range of displacements: a field study from the Atacama fault system, northern Chile," *Journal of Structural Geology*, vol. 31, no. 8, pp. 802–816, 2009.

[25] H. M. Savage and E. E. Brodsky, "Collateral damage: evolution with displacement of fracture distribution and secondary fault strands in fault damage zones," *Journal of Geophysical Research*, vol. 116, no. B3, 2011.

[26] J. E. Wilson, J. S. Chester, and F. M. Chester, "Microfracture analysis of fault growth and wear processes, Punchbowl Fault, San Andreas system, California," *Journal of Structural Geology*, vol. 25, no. 11, pp. 1855–1873, 2003.

[27] I. Korneva, A. Cilona, E. Tondi, F. Agosta, and M. Giorgioni, "Characterisation of the permeability anisotropy of Cretaceous platform carbonates by using 3D fracture modeling: the case study of Agri Valley fault zones (southern Italy)," *Italian Journal of Geosciences*, vol. 134, no. 3, pp. 396–408, 2015.

[28] M. Zambrano, E. Tondi, I. Korneva et al., "Fracture properties analysis and discrete fracture network modelling of faulted tight limestones, Murge Plateau, Italy," *Italian Journal of Geosciences*, vol. 135, no. 1, pp. 55–67, 2016.

[29] Z. K. Shipton, J. P. Evans, K. R. Robeson, C. B. Forster, and S. Snelgrove, "Structural heterogeneity and permeability in faulted eolian sandstone: implications for subsurface modeling of faults," *AAPG Bulletin*, vol. 86, pp. 863–883, 2002.

[30] M. Antonellini, A. Cilona, E. Tondi, M. Zambrano, and F. Agosta, "Fluid flow numerical experiments of faulted porous carbonates, Northwest Sicily (Italy)," *Marine and Petroleum Geology*, vol. 55, pp. 186–201, 2014.

[31] H. Fossen, R. A. Schultz, Z. K. Shipton, and K. Mair, "Deformation bands in sandstone: a review," *Journal of the Geological Society*, vol. 164, no. 4, pp. 755–769, 2007.

[32] E. Tondi, "Nucleation, development and petrophysical properties of faults in carbonate grainstones: evidence from the San Vito Lo Capo peninsula (Sicily, Italy)," *Journal of Structural Geology*, vol. 29, no. 4, pp. 614–628, 2007.

[33] G. Ballas, H. Fossen, and R. Soliva, "Factors controlling permeability of cataclastic deformation bands and faults in porous

sandstone reservoirs," *Journal of Structural Geology*, vol. 76, pp. 1–21, 2015.

[34] Q. J. Fisher and R. J. Knipe, "Fault sealing processes in siliciclastic sediments," *Geological Society, London, Special Publications*, vol. 147, no. 1, pp. 117–134, 1998.

[35] T. Ito and M. D. Zoback, "Fracture permeability and in situ stress to 7 km depth in the KTB scientific drillhole," *Geophysical Research Letters*, vol. 27, no. 7, pp. 1045–1048, 2000.

[36] K. Tadokoro and M. Ando, "Evidence for rapid fault healing derived from temporal changes inSwave splitting," *Geophysical Research Letters*, vol. 29, no. 4, p. 6-1, 2002.

[37] T. M. Mitchell and D. R. Faulkner, "Towards quantifying the matrix permeability of fault damage zones in low porosity rocks," *Earth and Planetary Science Letters*, vol. 339-340, pp. 24–31, 2012.

[38] Y. Nara, P. G. Meredith, T. Yoneda, and K. Kaneko, "Influence of macro-fractures and micro-fractures on permeability and elastic wave velocities in basalt at elevated pressure," *Tectonophysics*, vol. 503, no. 1-2, pp. 52–59, 2011.

[39] W. F. Brace, "Brittle fracture of rocks," in *State of Stress in the Earth's Crust*, W. R. Judd, Ed., pp. 110–178, Elsevier, New York, NY, USA, 1964.

[40] C. H. Scholz, "Microfracturing and the inelastic deformation of rock in compression," *Journal of Geophysical Research*, vol. 73, no. 4, pp. 1417–1432, 1968.

[41] M. H. Anders, S. E. Laubach, and C. H. Scholz, "Microfractures: a review," *Journal of Structural Geology*, vol. 69, pp. 377–394, 2014.

[42] K. Mizoguchi and K. Ueta, "Microfractures within the fault damage zone record the history of fault activity," *Geophysical Research Letters*, vol. 40, no. 10, pp. 2023–2027, 2013.

[43] M. Boccaletti, F. Calamita, G. Deiana et al., "Migrating foredeep-thrust belt systems in the northern Apennines and Southern Alps," *Palaeogeography, Palaeoclimatology, Palaeoecology*, vol. 77, no. 1, pp. 3–14, 1990.

[44] G. Gandolfi and L. Paganelli, "Il "Macigno costiero" fra La Spezia e Grosseto," *Giornali Geologiche*, vol. 54, no. 1, pp. 163–179, 1992.

[45] F. Mostardini and S. Merlini, *Appennino Centro-Meridionale. Sezioni geologiche e proposta di modello strutturale, vol. 24*, Memorie della Società Italiana, 1986.

[46] E. Patacca and P. Scandone, "Post-tortonian mountain building in the Apennines," in *Advances in Earth Science Research*, A. Boriani, M. Bonafede, G. B. Piccardo, and G. B. Vai, Eds., vol. 80, pp. 157–176, Atti Conv. Accademia dei Lincei, 1989.

[47] L. Carmignani, P. Conti, G. Cornamusini et al., "Geological map of Tuscany (Italy)," *Journal of Maps*, vol. 9, pp. 487–497, 2013.

[48] Istituto Superiore per la Protezione e la Riverca Ambientale, *Carta Geologica D'Italia, Agropoli Foglio 502, map, scale 1:10000*, Napoli, 1960.

[49] G. Gasperi, "Geologia del promontorio di Piombino (Livorno)," *Memorie della Società Italiana*, vol. 7, pp. 11–28, 1968.

[50] E. Mutti and F. Ricci Lucchi, "Le torbiditi dell'appennino settentrionale: Introduzione all'analisi di facies," *Memorie Societa Geologica Italiana*, vol. 11, pp. 161–199, 1972.

[51] R. Catanzariti, D. Rio, S. Chicchi, and G. Plesi, *Eta'e biostratigrafia a Nannofossili calcaeri delle Arenarie di M. Modino e del Macigno nell'alto Appennino reggianomodense*, vol. 56, Memorie Descrittive Carta Geologica d'Italia, 1991.

[52] A. Brogi, "Bowl-shaped basin related to low-angle detachment during continental extension: the case of the controversial Neogene Siena Basin (central Italy, Northern Apennines)," *Tectonophysics*, vol. 499, no. 1-4, pp. 54–76, 2011.

[53] G. Cornamusini, F. Elter, and F. Sandrelli, "The Corsica-Sardinia Massif as source area for the early northern Apennines foredeep system: evidence from debris flows in the "Macigno costiero" (Late Oligocene, Italy)," *International Journal of Earth Sciences*, vol. 91, no. 2, pp. 280–290, 2002.

[54] F. Mazzarini, G. Corti, P. Manetti, and F. Innocenti, "Strain rate and bimodal volcanism in the continental rift: Debre Zeyt volcanic field, northern MER, Ethiopia," *Journal of African Earth Sciences*, vol. 39, no. 3-5, pp. 415–420, 2004.

[55] G. Cornamusini, *An Integrated Approach to the Study of a Foredeep Basin: Lithostratigraphy, Sedimentology, Petrography and Nannofossils Biostratigraphy of the Southern Tuscan Macigno Turbidites, Northern Apennines, Italy. Abstract 15°*, I.A.S. Congress, Alicante, Spain, 1998.

[56] P. Orlandi, G. Corteccim, G. Protano, and F. Riccobono, "Mineral assemblages, stable isotopes and fluid inclusions in ore veins from the Macigno Formation at Calafuria (Livorno Mountains, northern Tuscany, Italy)," *Periodico di Mineralogia*, vol. 75, no. 1, pp. 73–84, 2006.

[57] R. Di Giulio and R. Valloni, "Sabbie e areniti, analisi ottica e classificazione: Analisi microscopica delle areniti terrigene: Paremetri metrologici e composizionali modeli," *Acta Naturalia Ateneo Parmense*, vol. 28, pp. 55–101, 1992.

[58] G. Cornamusini and A. Costantini, "Sedimentology of a Macigno turbidite section in the Piombino-Baratti area (northern Apennines, Italy)," *Giornali Geologi*, vol. 59, pp. 129–141, 1997.

[59] F. O. Amore, G. Bonardi, G. Ciampo, P. De Capoa, V. Perrone, and L. Sgrosso, "Relazioni tra "Flysch interni" e domini appenninici: reinterpretazione delle formazioni di Pollica, San Mauro e Albidona nel quadro della evoluzione inframiocenica delle zone esterne appenniniche," *Memorie della Società Geologica Italiana*, vol. 41, pp. 285–297, 1998.

[60] R. W. H. Butler and W. D. McCaffrey, "Structural evolution and sediment entrainment in mass-transport complexes: outcrop studies from Italy," *Journal of the Geological Society*, vol. 167, no. 3, pp. 617–631, 2010.

[61] A. Cammarosano, G. Cavuoto, M. Danna et al., "Nuovi dati e nuove interpretazioni sui flysch terrigeni del Cilento (Appennino meridionale, Italia)," *Bolletino della Società Geologica Italiana*, vol. 119, pp. 395–405, 2004.

[62] M. Fonnesu, P. Haughton, F. Felletti, and W. McCaffrey, "Short length-scale variability of hybrid event beds and its applied significance," *Marine and Petroleum Geology*, vol. 67, pp. 583–603, 2015.

[63] G. Cavuoto, L. Martelli, G. Nardi, and A. Valente, "Depositional systems and architecture of Olgio-Miocene turbidite successions in Cilento (Southern Apennines)," *GeoActa*, vol. 3, pp. 129–147, 2005.

[64] S. Vitale, S. Ciarcia, S. Mazzoli, A. Iannace, and M. Torre, "Structural analysis of the 'Internal' Units of *Cilento*, Italy: new constraints on the Miocene tectonic evolution of the southern Apennine accretionary wedge," *Comptes Rendus Geoscience*, vol. 342, no. 6, pp. 475–482, 2010.

[65] S. Critelli and E. Le Pera, "Detrital modes and provenance of Miocene sandstones and modern sands to the Southern Apennines thrust-top basins (Italy)," *Journal of Sedimentary Research*, vol. 64, no. 4a, pp. 824–835, 1994, A64.

[66] G. Cavuoto, L. Martelli, G. Nardi, and A. Valente, "Turbidite depositional systems and architectures, Cilento, Italy," in *Atlas of Deep-Water Outcrops*, T. H. Nilsen, R. D. Shew, G. S. Steffens, and J. R. J. Studlick, Eds., vol. 56, AAPG Studies in Geology, 2007.

[67] F. O. Amore, G. Ciampo, P. De Capoa, and E. Ruggero, "Problemi biostratigrafici dei sedimenti terrigeni nell'Appennino meridionale," *Memorie della Società Geologica Italiana*, vol. 41, pp. 621–625, 1998.

[68] M. Russo, A. Zuppetta, and A. Guida, *Alcune precisazioni stratigrafiche sul Flysch del Cilento (Appennino meridionale)*, vol. 114, Bolletino della Società Geologica Italiana, 1995.

[69] F. Balsamo, F. Storti, F. Salvini, A. T. Silva, and C. C. Lima, "Structural and petrophysical evolution of extensional fault zones in low-porosity, poorly lithified sandstones of the Barreiras Formation, NE Brazil," *Journal of Structural Geology*, vol. 32, no. 11, pp. 1806–1826, 2010.

[70] E. Tondi, A. Rustichelli, A. Cilona et al., "Hydraulic properties of fault zones in porous carbonates, examples from central and southern Italy," *Italian Journal of Geosciences*, vol. 135, no. 1, pp. 68–79, 2016.

[71] C. M. Filomena, J. Hornung, and H. Stollhofen, "Assessing accuracy of gas-driven permeability measurements: a comparative study of diverse Hassler-cell and probe permeameter devices," *Solid Earth*, vol. 5, no. 1, pp. 1–11, 2014, v.

[72] C. A. Leon, "New perspectives in mercury porosimetry," *Advances in Colloid and Interface Science*, vol. 76-77, pp. 341–372, 1998.

[73] A. Cilona, D. R. Faulkner, E. Tondi et al., "The effects of rock heterogeneity on compaction localization in porous carbonates," *Journal of Structural Geology*, vol. 67, pp. 75–93, 2014, v.

[74] F. Arzilli, A. Cilona, L. Mancini, and E. Tondi, "Using synchrotron X-ray microtomography to characterize the pore network of reservoir rocks: a case study on carbonates," *Advances in Water Resources*, vol. 95, pp. 254–263, 2016.

[75] M. Zambrano, E. Tondi, L. Mancini et al., "3D pore-network quantitative analysis in deformed carbonate grainstones," *Marine and Petroleum Geology*, vol. 82, pp. 251–264, 2017.

[76] D. Zandomeneghi, M. Voltolini, L. Mancini, F. Brun, D. Dreossi, and M. Polacci, "Quantitative analysis of X-ray microtomography images of geomaterials: application to volcanic rocks," *Geosphere*, vol. 6, no. 6, pp. 793–804, 2010.

[77] O. Gharbi and M. J. Blunt, "The impact of wettability and connectivity on relative permeability in carbonates: a pore network modeling analysis," *Water Resources Research*, vol. 48, no. 12, 2012.

[78] M. J. Blunt, B. Bijeljic, H. Dong et al., "Pore-scale imaging and modelling," *Advances in Water Resources*, vol. 51, pp. 197–216, 2013.

[79] M. Zambrano, E. Tondi, L. Mancini et al., "Fluid flow simulation and permeability computation in deformed porous carbonate grainstones," *Advances in water resources*, vol. 115, pp. 95–111, 2018.

[80] Í. B. da Silva, "X-ray computed microtomography technique applied for cementitious materials: a review," *Micron*, vol. 107, pp. 1–8, 2018.

[81] A. Abrami, F. Arfelli, R. C. Barroso et al., "Medical applications of synchrotron radiation at the SYRMEP beamline of ELETTRA," *Nuclear Instruments and Methods in Physics Research*, vol. 548, no. 1-2, pp. 221–227, 2005.

[82] G. Tromba, R. Longo, A. Abrami et al., "The SYRMEP beamline of elettra: clinical mammography and bio-medical applications," in *AIP Conference Proceedings*, vol. 1266, pp. 18–23, Melbourne, Australia, 2010.

[83] P. Cloetens, R. Barrett, J. Baruchel, J. P. Guigay, and M. Schlenker, "Phase objects in synchrotron radiation hard X-ray imaging," *Journal of Physics D: Applied Physics*, vol. 29, no. 1, pp. 133–146, 1996.

[84] D. R. Baker, L. Mancini, M. Polacci et al., "An introduction to the application of X-ray microtomography to the three-dimensional study of igneous rocks," *Lithos*, vol. 148, pp. 262–276, 2012.

[85] F. Brun, S. Pacilè, A. Accardo et al., "Enhanced and flexible software tools for x-ray computed tomography at the Italian synchrotron radiation facility Elettra," *Fundamental Informaticae*, vol. 141, no. 2-3, pp. 233–243, 2015.

[86] W. Palenstijn, K. Batenburg, and J. Sijbers, "Performance improvements for iterative electron tomography reconstruction using graphics processing units (GPUs)," *Journal of Structural Biology*, vol. 176, no. 2, pp. 250–253, 2011.

[87] D. Gürsoy, F. De Carlo, X. Xiao, and C. Jacobsen, "TomoPy: a framework for the analysis of synchrotron tomographic data," *Journal of Synchrotron Radiation*, vol. 21, no. 5, pp. 1188–1193, 2014.

[88] D. Paganin, S. C. Mayo, T. E. Gureyev, P. R. Miller, and S. W. Wilkins, "Simultaneous phase and amplitude extraction from a single defocused image of a homogeneous object," *Journal of Microscopy*, vol. 206, no. 1, pp. 33–40, 2002.

[89] F. Brun, L. Mancini, P. Kasae, S. Favretto, D. Dreossi, and G. Tromba, "Pore3D: a software library for quantitative analysis of porous media," *Nuclear Instruments and Methods in Physics Research Section A: Accelerators, Spectrometers, Detectors and Associated Equipment*, vol. 615, no. 3, pp. 326–332, 2010.

[90] C. Tomasi and R. Manduchi, "Bilateral filtering for gray and color images," in *Sixth International Conference on Computer Vision*, pp. 839–846, New Delhi, India, 1998.

[91] J. A. Hartigan and M. A. Wong, "Algorithm AS 136: a K-means clustering algorithm," *Applied Statistics*, vol. 28, no. 1, pp. 100–108, 1979.

[92] J. Kozeny, *Uber Kapillare Leitung des Wassers im Boden, Sitzungsber*, vol. 136, Akad. Wiss. Wien, Math. Naturw Klasse, 1927, Abt.II A.

[93] P. C. Carman, "Fluid flow through granular beds," *Transactions of the American Institute of Chemical Engineers*, vol. 15, p. 150, 1937.

[94] H. J. G. Gundersen, R. W. Boyce, J. R. Nyengaard, and A. Odgaard, "The Conneulor: unbiased estimation of connectivity using physical disectors under projection," *Bone*, vol. 14, no. 3, pp. 217–222, 1993.

[95] B. R. Crawford, "Experimental fault sealing: shear band permeability dependency on cataclastic fault gouge characteristics," *Geological Society, London, Special Publications*, vol. 127, no. 1, pp. 27–47, 1998.

[96] S. Uehara and M. Takahashi, "How rock mechanical properties affect fault permeability in Neogene mudstone?," *Energy Procedia*, vol. 37, pp. 5588–5595, 2013.

[97] E. Scholz, *The Mechanics of Earthquakes and Faulting*, Cambridge Univeristy Press, Cambridge, New York, Port Chester, Melbourne, Sydney, 1990.

[98] A. G. Hull, "A late Holocene marine terrace on the Kidnappers coast, North Island, New Zealand: some implications for shore platform development processes and uplift mechanism," *Quaternary Research*, vol. 28, no. 02, pp. 183–195, 1987.

[99] M. R. Heynekamp, L. B. Goodwin, P. S. Mozley, and W. C. Haneberg, "Controls on fault-zone architecture in poorly lithified sediments, Rio Grande Rift, New Mexico: implications for fault-zone permeability and fluid flow," *Faults and Subsurface Fluid Flow in the Shallow Crust*, vol. 113, pp. 27–49, 1999.